

Spatial Characterization of Holographic MIMO Channels

Andrea Pizzo, *Member, IEEE*, Thomas L. Marzetta, *Fellow, IEEE*, Luca Sanguinetti,
Senior Member, IEEE

Abstract

Imagine beings surrounded by continuous apertures that can emit and receive electromagnetic waves. A system of this sort, having an uncountably infinite number of antennas in a compact space, is called Holographic MIMO. Given the solid results for Massive MIMO, one might expect a holographic system to realize extreme spatial resolution, incredible energy efficiency, and unprecedented spectral efficiency. At present, however, the fundamental advantages of continuous apertures over conventional discrete spaced antenna arrays have not been conclusively established. A major challenge for the analysis and understanding of such a paradigm shift is the lack of mathematically tractable and numerically reproducible spatially-continuous channel models that retain some semblance of the physical reality. Physical models are too complex for tractable analysis. This paper aims to take a closer look at this challenge through the conventional tools of linear systems theory and Fourier transform. Notably, this leads to a rather simple Fourier plane-wave spectral representation of a three-dimensional spatially-continuous channel from which a computationally efficient way to generate samples over compact continuous apertures can be developed.

I. INTRODUCTION

Massive MIMO refers to a wireless network technology where the base stations are equipped with a very large number N of antennas to serve a multitude of K terminals by spatial multiplexing [2]. Thanks to the solid results developed over the last decade, Massive MIMO is today a mature technology [3], [4] whose key ingredients have made it into the 5G New Radio standard [5]. Its advantages in terms of spectral efficiency [6], energy efficiency [7] and power control [8] are well understood and recognized. The long-standing pilot contamination issue [3], [9], which was believed to impose a fundamental limitation, has also been finally resolved [10] and the channel capacity was shown to increase theoretically unboundedly in the regime where $N \rightarrow \infty$ while K is fixed. Hence, a natural question is: *how can we practically approach the limit $N \rightarrow \infty$?* One solution

Part of this work was presented at ISIT18 [1]. A. Pizzo and T. Marzetta are with the Department of Electrical and Computer Engineering, Tandon School of Engineering, 11201 Brooklyn, NY (andrea.pizzo@nyu.edu, tom.marzetta@nyu.edu). L. Sanguinetti is with the Dipartimento di Ingegneria dell'Informazione, University of Pisa, 56122 Pisa, Italy (luca.sanguinetti@unipi.it).

is to integrate an uncountably infinite number of antennas into a compact space, in the form of a spatially continuous electromagnetic aperture. Research in this field is taking place under the names of holographic radio-frequency system [11], and large intelligent surfaces [12]. The technology developed in [13], known as holographic beamforming, is the first step in this direction. We refer to these different technologies as *Holographic MIMO* since a spatially continuous electromagnetic aperture is the ultimate form of a spatially-constrained MIMO array as $N \rightarrow \infty$.

A. Motivation

The MIMO channel between transmit and receive arrays is typically described by a discrete space-time random field [14], [15]. This modeling approach has been extensively used in MIMO and Massive MIMO, with either a countably finite or infinite number of antennas. In Massive MIMO, e.g., it has been used for its asymptotic analysis in the regime where $N \rightarrow \infty$ and K is fixed [2], [6], [10], but also in the case where $N, K \rightarrow \infty$ with a fixed ratio [16]–[18]. The vast majority of these conventional channel models have a two-fold limitation when applied to the study of a Holographic MIMO system:

- 1) As N increases, they typically assume that the array aperture increases and all antennas contribute. This is clearly impossible for two reasons:¹ (i) practical arrays have a spatially-constrained topology; (ii) one would eventually receive more power than it was transmitted;
- 2) They are statically characterized by the spatial correlation matrix (e.g., [4, Sec. 2.2]), which depends jointly on the physical propagation environment and array geometry (e.g., [4, Sec. 7.3]). This makes it hard to infer the physical properties of the propagation environment as N increases. For example, arrays with larger antenna spacing in a less scattered environment yield the same spatial correlation as arrays with smaller antenna spacing but in a more scattered environment [20], [21]. Moreover, the spatial correlation matrix is often modeled to be analytically tractable and thus lacks a direct connection to the underlying wireless propagation mechanisms.

In the Massive MIMO literature, the first limitation is addressed in [22], [23], e.g., where the authors focus on a practical, spatially-constrained array topology, and show that, unlike in [2], the so-called non-coherent interference does not vanish as $N \rightarrow \infty$. However, such papers still suffer from the second limitation. The decoupling of the physical propagation environment from the array

¹Therefore, it must be clear that the asymptotic analyses in [2], [6], [10], [16]–[18] can only be used to understand the scaling behavior of Massive MIMO for a practical number of antennas [19], but cannot be used to study its fundamental physical limit.

geometry can be obtained by recurring to the modeling of spatially-continuous electromagnetic apertures [12], [20], [21]. The reception of a complex-valued electromagnetic field over a planar continuous surface is studied in [12] under a perfect line-of-sight (LoS) propagation. This leads to a simple deterministic channel model, which is then used to evaluate the system capacity and compute the degrees of freedom (DoF) of the channel. In practice, however, propagation from an electromagnetic source to a receive aperture takes place through a multiplicity of paths. This creates the so-called non-line-of-sight (NLoS) stochastic propagation environment [24]. The simplest NLoS scenario is when scalar radio waves are considered (i.e., no polarization), and the receiving aperture is located deep inside a homogeneous and isotropic (i.e., no dominant spatial directivity) scattering medium [25]. This propagation model is widely known as Clarke's isotropic scattering model; see [26] and [27] for a two-dimensional (2D) and three-dimensional (3D) analysis, respectively. A direct consequence of this model is that the autocorrelation function between two arbitrary points in 2D and 3D spaces at a distance R is respectively equal to $J_0(2\pi R/\lambda)$ and $\text{sinc}(2R/\lambda)$ with λ being the wavelength [15], [24]; that is, the communication channel exhibits spatial correlation even if there is no dominant spatial directivity.

The aim of this paper is to generalize Clarke's model to non-isotropic random scattering environments, with the purpose to obtain a 3D NLoS stochastic spatially-continuous channel model, which is: (i) mathematically tractable; and (ii) numerically reproducible. These are two desirable properties of any stochastic channel model. Previous works in the field of spatial characterization of non-isotropic NLoS spatially-continuous channel models can be found in [20], [21] and [28]. Unlike these works, we treat radio wave propagation as a linear system, which provides us with a simple and intuitive interpretation of the proposed model through linear system theory and Fourier transform, without the recourse to special functions (i.e., Green function [20], [21], spherical harmonics [28]), detailed parametric models, and unfamiliar subsidiary mathematical results.

B. Contribution

Following the common treatment in MIMO communications [14], we model the propagation of a 3D complex-valued electromagnetic scalar field through a random scattering environment as the product of large-scale fading — representing shadow fading and range-dependent attenuation — and small-scale fading — changing on a scale comparable to a wavelength. This paper only considers the small-scale fading, which we simply refer to as *channel* in what follows. We treat it as a zero-mean, spatially-stationary, and Gaussian scalar random field satisfying the scalar wave

equation (equivalent to the Helmholtz equation, in the temporal-frequency domain), as dictated by physics. This requirement implies that the power spectral density is an impulsive function with support on the surface of a sphere of radius $\kappa = 2\pi/\lambda$, and it is uniquely described by one single function, i.e., the *spectral factor*, which physically describes the propagation environment.

By exploiting the analogy with time-domain Gaussian random processes, we first describe the channel over an infinitely large spatially-continuous aperture by a Fourier plane-wave spectral representation given by a superposition of a continuum of *plane-waves* having statistically-independent Gaussian-distributed random coefficients. Then, we show that, along any spatial cut-set, the Helmholtz equation acts as a linear space-time invariant physical filter, which makes the channel bandlimited to a disk of radius κ and the Fourier plane-wave spectral representation is essentially 2D. Finally, we leverage the above results to statistically characterize the channel over a large, but finite, spatially-continuous aperture by a 2D Fourier plane-wave series representation. This representation is used to obtain a numerical procedure to efficiently generate spatial channel samples through the inverse fast Fourier transform (IFFT).

C. Outline and Notation

The rest of this paper is organized as follows. Section II introduces the 3D continuous model for the small-scale fading and studies the implication of the Helmholtz equation on channel statistics. Section III computes the Fourier plane-wave spectral representation for an infinitely large spatially-continuous aperture. Section IV provides a linear-system theoretic interpretation of the channel and shows the connection to Clarke's isotropic channel model. Section V derives the Fourier plane-wave series representation for a large, but finite, spatially-continuous aperture, which is used to numerically generate spatial samples of the channel. The numerical method is validated by means of Monte Carlo simulations. Section VI concludes with a general discussion and outlook on the developed analytical framework.

We will use upper (lower) case letters for frequency (time) entities. We use calligraphic letters for indicating sets and boldfaced lower case letters for vectors. For a given vector \mathbf{r} , $\hat{\mathbf{r}}$ is a unit vector denoting its direction. $\mathbb{E}\{\cdot\}$ denotes the expectation operator. The notation $n \sim \mathcal{N}_{\mathbb{C}}(0, \sigma^2)$ stands for a circularly-symmetric Gaussian variable with variance σ^2 . We use \mathbb{R}^n and \mathbb{Z}^n to denote the n -dimensional real-valued and integer-valued vector spaces. The notation \mathbb{R}_+ and \mathbb{Z}_+ is used for the non-negative real-valued and non-negative integer-valued vector spaces. The notation $\nabla^2 = \frac{\partial^2}{\partial x^2} + \frac{\partial^2}{\partial y^2} + \frac{\partial^2}{\partial z^2}$ is the

scalar Laplace operator. $\mathbb{1}_{\mathcal{X}}(x)$ is the indicator function of a subset $x \in \mathcal{X}$. $\lceil x \rceil$ gives the smallest integer equal to or greater than x . $\delta(x)$ is the Dirac delta function while δ_n is the Kronecker delta.

II. PHYSICS-BASED CONTINUOUS CHANNEL MODELING

We start revisiting the fundamental implications of the homogeneous wave equation on the modeling of a 3D scalar random channel. In a homogeneous, isotropic, source-free, and scattered infinite medium each of the three Cartesian components $(E_x, E_y, E_z) \in \mathbb{C}^3$ of the electrical field $\mathbf{E} = E_x \hat{\mathbf{x}} + E_y \hat{\mathbf{y}} + E_z \hat{\mathbf{z}}$ can be described independently by the scalar wave equation [29] and electromagnetic waves behave in a manner similar to that of acoustic waves [1]. The spatially-continuous wireless channel measured over an *infinitely large* spatially-continuous rectangular volume aperture can thus be modeled as a *space-time scalar random field* [15]

$$\{h(x, y, z, t) : (x, y, z) \in \mathbb{R}^3, t \in (-\infty, \infty)\}. \quad (1)$$

A primary interest in wireless communications lies in scenarios in which h can be modeled as a zero-mean, spatially-stationary and Gaussian random field [1]. The Gaussian assumption is considered valid whenever the distance between scattering events is large compared to the wavelength λ , but small compared to the distance between source and receiver [25].

A. Helmholtz Equation

The electromagnetic nature of the wireless channel requires each realization of h to satisfy the homogeneous scalar wave equation with probability 1 [29, Eq. (1.2.17)]:

$$\left(\nabla^2 - \frac{1}{c^2} \frac{\partial^2}{\partial t^2} \right) h(x, y, z, t) = 0 \quad (2)$$

which is a second-order linear partial differential equation. Along any spatial cut-set, the wave equation acts as a linear space-time invariant physical filter; that is, the linear combination of any two solutions is a solution and a time-delayed, or space-shifted version of h is also a solution.² This observation allows us to treat the wave propagation phenomena by using the linear-system theory. For any point in space, h can be equivalently expressed in terms of its frequency-domain analog $h_\omega(x, y, z)$ with $\omega \in (-\infty, \infty)$ through the Fourier transform relation

$$h_\omega(x, y, z) = \int_{-\infty}^{\infty} h(x, y, z, t) e^{-i\omega t} dt. \quad (3)$$

²This because the second-order differential operator is linear and translation-invariant.

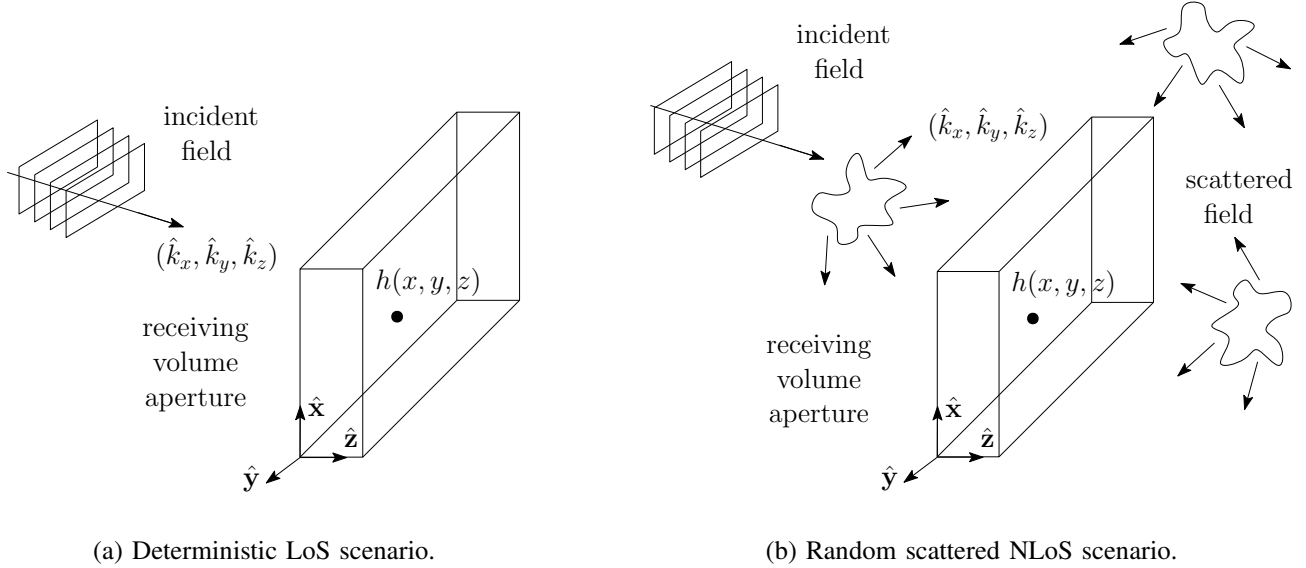


Fig. 1: Electromagnetic wave propagation in a 3D environment.

In this paper, we restrict our analysis to monochromatic waves, i.e., propagating at the same single frequency ω , and leave the general frequency-wavenumber analysis for future works. Thus, we omit the subscript in (3) and call $h(x, y, z) = h_\omega(x, y, z)$. From (3), the homogeneous scalar wave equation in frequency-domain, also known as the Helmholtz equation, is obtained as:

$$(\nabla^2 + \kappa^2) h(x, y, z) = 0 \quad (4)$$

where we define the wavenumber as

$$\kappa = \frac{\omega}{c} = \frac{2\pi}{\lambda} \quad (5)$$

with c being the speed of light. Thus, κ is the angular displacement (in radians) per unit of length.

B. General Homogeneous Plane-wave Solution

A solution (with probability 1) to (4) is given by [29, Eq. (1.2.23)]:

$$h(x, y, z) = H e^{i(k_x x + k_y y + k_z z)}, \quad (k_x, k_y, k_z) \in \mathcal{S}(\kappa) \quad (6)$$

where $H \in \mathbb{C}$, and $(k_x, k_y, k_z) \in \mathbb{R}^3$ are the real-valued Cartesian coordinates in the wavenumber-domain, which are confined to the support

$$\mathcal{S}(\kappa) = \{(k_x, k_y, k_z) \in \mathbb{R}^3 : k_x^2 + k_y^2 + k_z^2 = \kappa^2\} \quad (7)$$

of an impulsive sphere of radius κ centered on the origin (see Fig. 2a). The *wavenumber* (also known as spatial-frequency) plays the same role as the angular frequency when computing the Fourier transform of time-domain signals [30]. Indeed, the spatial and wavenumber domains represent the

time and frequency counterparts, respectively. The formula in (6) describes a single *plane-wave* impinging on the spatial point (x, y, z) for which its wavefronts form infinite planes all oriented towards a propagating direction $(\hat{k}_x, \hat{k}_y, \hat{k}_z) = (\frac{k_x}{\kappa}, \frac{k_y}{\kappa}, \frac{k_z}{\kappa}) \in \mathcal{S}(1)$ (see Fig. 1a) [29]. The condition $(k_x, k_y, k_z) \in \mathcal{S}(\kappa) \subset \mathbb{R}^3$ excludes the so-called *evanescent waves*, which decay exponentially fast in space and do not contribute to the far-field propagation. The solution in (6) has been used in [12, Eq. (5)] to model the LoS propagation scenario and leads to a deterministic channel model that follows from standard geometrical considerations.

Differently, in a random scattering environment as illustrated in Fig. 1b, there will be an *uncountably infinite* number of plane-waves each one of which impinges on (x, y, z) from a direction $(\hat{k}_x, \hat{k}_y, \hat{k}_z)$ and has a complex-valued Gaussian-distributed random amplitude $H(k_x, k_y, k_z)$. By exploiting the linearity of the Laplacian operator, a generalized solution to (4) can be obtained as a linear combination of plane-waves:³

$$h(x, y, z) = \iiint_{\mathcal{S}(\kappa)} H(k_x, k_y, k_z) e^{i(k_x x + k_y y + k_z z)} dk_x dk_y dk_z \quad (8)$$

which is a *general homogeneous plane-wave* solution to the Helmholtz equation (e.g., [31, Ch. 6.7]). The above formula acts as a continuous *plane-wave decomposition* of the channel and it is reminiscent of a 3D inverse Fourier transform. In fact, Fourier integral representations are referred to as *plane-wave representations* in physics [29], [31]. Notice that the plane-wave interpretation naturally appears as a general solution to the Helmholtz equation in (4). In fact, complex exponentials are essentially the eigenfunctions of every translation invariant operator [32]. As a major contribution of this paper, we aim to statistically characterize the plane-wave amplitudes H in (8) for a general non-isotropic random scattering environment.

C. Fourier Spectral Representation

Since h is modeled as a zero-mean, spatially-stationary and Gaussian random field, its spatial autocorrelation function

$$c_h(x, y, z) = \mathbb{E}\{h^*(x', y', z')h(x + x', y + y', z + z')\} \quad (9)$$

between every pair of points constitutes a complete statistical description, where the expectation is taken with respect to the channel realizations. We focus on the class of second-order⁴ random fields

³Notice that the integral representation in (8) is due to the continuity of the wavenumber support $\mathcal{S}(\kappa)$ in (7).

⁴A second-order random variable h is one which satisfies $\mathbb{E}\{|h|^2\} < \infty$. A collection of second-order random variables over $(x, y, z) \in \mathbb{R}^3$ is a second-order spatial random field $h(x, y, z)$ [33, Ch. 2].

that have finite average power $c_h(0, 0, 0) = P_h < \infty$. Therefore, h can also be statistically described in the wavenumber domain by its real-valued power spectral density, which is found through the Wiener-Khinchin theorem

$$S_h(k_x, k_y, k_z) = \iiint_{-\infty}^{\infty} c_h(x, y, z) e^{-i(k_x x + k_y y + k_z z)} dx dy dz \quad (10)$$

or equivalently,

$$c_h(x, y, z) = \frac{1}{(2\pi)^3} \iiint_{-\infty}^{\infty} S_h(k_x, k_y, k_z) e^{i(k_x x + k_y y + k_z z)} dk_x dk_y dk_z \quad (11)$$

which may be obtained from the canonical time-frequency domain formulation by replacing the *time-frequency* map with its *space-wavenumber* counterpart. The power spectral density plays a key role in the mapping between these two domains, and particularly in the computation of the plane-wave amplitudes in (8), which are thus given by

$$H(k_x, k_y, k_z) = \sqrt{S_h(k_x, k_y, k_z)} W(k_x, k_y, k_z) \quad (12)$$

where W is a zero-mean stationary white-noise Gaussian random field with unit spectrum, and S_h is the power spectral density as defined in (10). Plugging (12) into (8) yields

$$h(x, y, z) = \frac{1}{(2\pi)^{3/2}} \iiint_{\mathcal{S}(\kappa)} \sqrt{S_h(k_x, k_y, k_z)} W(k_x, k_y, k_z) e^{i(k_x x + k_y y + k_z z)} dk_x dk_y dk_z \quad (13)$$

which is a superposition of an uncountably-infinite number of plane-waves having statistically-independent Gaussian-distributed random amplitudes. The factor $(2\pi)^{-3/2}$ is introduced for normalization purposes. Notice that (13) is known in the statistical literature as *Fourier spectral representation* [30], [32] and provides a statistical description of h in the wavenumber domain. Broadly, every deterministic signal of finite energy can be represented either in the time domain as a waveform or in the frequency domain as a spectrum. The mapping between these two domains is the Fourier transform. Similarly, every second-order, stationary random process can be represented either in time domain or in frequency domain through the Fourier spectral representation. In Appendix A we revise this representation and show that it can be applied to spatially-stationary random fields.

D. Implications of the Helmholtz Equation

Now, by applying the Laplacian operator to both sides of (9) and interchanging the order of integration and derivation, we have that

$$\nabla^2 c_h(x, y, z) + \kappa^2 c_h(x, y, z) = 0 \quad (14)$$

which implies that the spatial autocorrelation c_h itself satisfies the Helmholtz equation [1]. This observation is instrumental to characterize the power spectral density S_h in (10). In fact, by inserting the inverse Fourier transform (11) into (14) and interchanging the order of integration and differentiation we obtain

$$(k_x^2 + k_y^2 + k_z^2 - \kappa^2) S_h(k_x, k_y, k_z) = 0 \quad (15)$$

which implies that S_h vanishes everywhere except on the wavenumber support $\mathcal{S}(\kappa)$ in (7), as expected. Nevertheless, being S_h defined on a support with zero measure, it cannot be interpreted as an ordinary function, but rather as a singular Delta distribution [34]. Notice that if S_h was treated in the ordinary sense as a function defined on a sphere, the evaluation of (13) would lead to a zero integral, since the support would have zero measure. Moreover, since any two distributions that are identical except for a set of zero measure returns the same Lebesgue integral [35], the following result is established.

Lemma 1. *The power spectral density of any $h(x, y, z)$ obeying (4) is in the form⁵*

$$S_h(k_x, k_y, k_z) = A_h^2(k_x, k_y, k_z) \delta(k_x^2 + k_y^2 + k_z^2 - \kappa^2) \quad (16)$$

where A_h is a real-valued non-negative function called spectral factor.

Hence, we define *3D physics-based channel* any h whose power spectral density S_h is of the form in (16). Interestingly, (13) can be interpreted as the homogeneous solution of the stochastic partial differential Helmholtz equation in (4), with boundary conditions specified by (16).

III. FOURIER DESCRIPTION OF PHYSICS-BASED CHANNELS

Unfortunately, the direct evaluation of h through (13) requires the computation of the square-root of the impulsive function S_h in (16), which makes the standard Fourier spectral representation in (13) inadequate to statistically describe physics-based channels (even in the sense of distributions). To obtain a mathematically tractable expression of h , in what follows we start by taking the Fourier inversion of S_h with respect to one of its arbitrary wavenumber component, say $k_z \in \mathbb{R}$, while the other two are held constant. This allows to eliminate the issue related to the Dirac delta function. The Fourier inversion to the other two wavenumber components yields the autocorrelation function c_h from which a closed-form expression for the channel is obtained.

⁵The interpretation of a Dirac delta function having an argument which is a non-linear function is discussed in [36].

A. Fourier inversion of $S_h(k_x, k_y, k_z)$ in k_z

From (10), we obtain

$$\frac{1}{2\pi} \int_{-\infty}^{\infty} S_h(k_x, k_y, k_z) e^{ik_z z} dk_z = \iint_{-\infty}^{\infty} c_h(x, y, z) e^{-i(k_x x + k_y y)} dx dy. \quad (17)$$

Since the three wavenumbers are confined to the wavenumber sphere $\mathcal{S}(\kappa)$, k_z is determined, apart from a sign, by the other two (k_x, k_y) . Notice that the composition of the Dirac delta with a differentiable function $g(k_z) = k_z^2 - (\kappa^2 - k_x^2 - k_y^2)$ can be rewritten as [37, Eq. (181.a)]

$$\delta(k_z^2 - (\kappa^2 - k_x^2 - k_y^2)) = \frac{\delta(k_z - k_{z,0}) + \delta(k_z + k_{z,0})}{2 k_{z,0}} \quad (18)$$

where we define

$$k_{z,0} = \sqrt{\kappa^2 - k_x^2 - k_y^2}. \quad (19)$$

Since we only consider plane-waves for which $k_z \in \mathbb{R}$, from (19) it follows that the wavenumber coordinates (k_x, k_y) have compact support given by

$$\mathcal{D}(\kappa) = \{(k_x, k_y) \in \mathbb{R}^2 : k_x^2 + k_y^2 \leq \kappa^2\} \quad (20)$$

which is a disk of radius κ centered on the origin. Let us denote with $A_{h,\pm}^2(k_x, k_y) = A_h^2(k_x, k_y, \pm k_{z,0})$ the values assumed by the spectral factor at the two wavenumber points $k_z = \pm k_{z,0}$ along the axis k_z (see Fig. 2a). The use of (16) as well as (18)–(20) into (17) yields

$$\frac{1}{2\pi} \int_{-\infty}^{\infty} S_h(k_x, k_y, k_z) e^{ik_z z} dk_z = S_h^+(k_x, k_y) e^{ik_{z,0} z} + S_h^-(k_x, k_y) e^{-ik_{z,0} z} \quad (21)$$

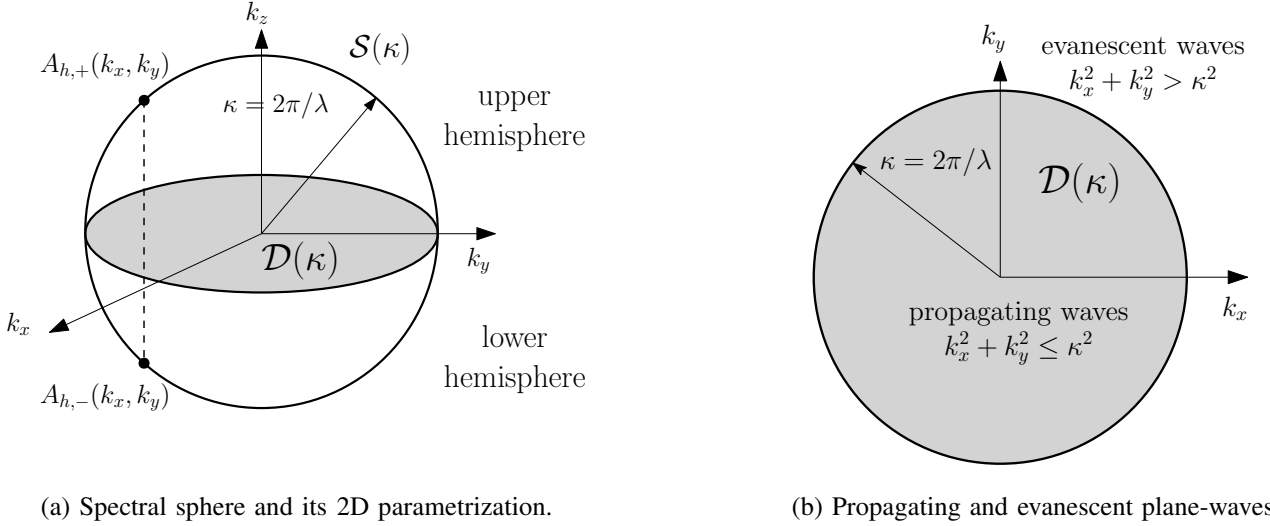
which is the sum of the two 2D power spectral densities

$$S_h^{\pm}(k_x, k_y) = \frac{A_{h,\pm}^2(k_x, k_y)/4\pi}{\sqrt{\kappa^2 - k_x^2 - k_y^2}}, \quad (k_x, k_y) \in \mathcal{D}(\kappa) \quad (22)$$

where we have replaced $k_{z,0}$ with its expression in (19). Thus, S_h^{\pm} are the parametrization of S_h on the upper and lower hemispheres of $\mathcal{S}(\kappa)$ on the 2D wavenumber disk support $\mathcal{D}(\kappa)$. The Fourier inversion of (21) to the other two wavenumber components (k_x, k_y) provides a closed-form expression for the autocorrelation function of h :

$$c_h(x, y, z) = \frac{1}{(2\pi)^2} \iint_{-\infty}^{\infty} [S_h^+(k_x, k_y) e^{ik_{z,0} z} + S_h^-(k_x, k_y) e^{-ik_{z,0} z}] e^{i(k_x x + k_y y)} dk_x dk_y \quad (23)$$

which is easily verified to satisfy the Helmholtz equation in (14). This intermediate result leads to an integral representation of h that overcomes the problem encountered in (13).



(a) Spectral sphere and its 2D parametrization.

(b) Propagating and evanescent plane-waves.

Fig. 2: Wavenumber support of the power spectral density of the channel $h(x, y, z)$.

B. The 2D Fourier Plane-Wave Spectral Representation

By inspection of (23), one may generate h by taking the square root of the two power spectral densities S_h^\pm and multiplying each of the resulting amplitudes by two 2D independent, zero-mean, complex-valued, white-noise Gaussian random fields with unit variance $W^\pm(k_x, k_y) = W(k_x, k_y, \pm k_{z,0})$ that capture the randomness of the scattering environment. This yields the following 2D Fourier plane-wave spectral representation of the 3D channel [1]

$$h(x, y, z) = h_+(x, y, z) + h_-(x, y, z) \quad (24)$$

with

$$h_\pm(x, y, z) = \frac{1}{4\pi\sqrt{\pi}} \iint_{\mathcal{D}(\kappa)} \frac{A_{h,\pm}(k_x, k_y)}{(\kappa^2 - k_x^2 - k_y^2)^{1/4}} W^\pm(k_x, k_y) e^{i(k_x x + k_y y \pm \sqrt{\kappa^2 - k_x^2 - k_y^2} z)} dk_x dk_y \quad (25)$$

where we replaced $k_{z,0}$ with its expression in (19). For each $(k_x, k_y) \in \mathcal{D}(\kappa)$ the integrands h_\pm respectively describe two plane-waves spatially propagating in the half-spaces $z > 0$ and $z < 0$ and satisfying the Helmholtz equation independently, which in turn implies that (24) also satisfies the Helmholtz equation. Thus, the effect of any Cartesian component of the electromagnetic field in any infinite z -plane can be exactly represented by a superposition of upgoing and downgoing plane-waves having statistically independent Gaussian-distributed random amplitudes

$$H(k_x, k_y, \pm k_{z,0}) = H_\pm(k_x, k_y) = \begin{cases} \frac{A_{h,\pm}(k_x, k_y) W^\pm(k_x, k_y)}{4\pi\sqrt{\pi}(\kappa^2 - k_x^2 - k_y^2)^{1/4}} & (k_x, k_y) \in \mathcal{D}(\kappa) \\ 0 & \text{elsewhere.} \end{cases} \quad (26)$$

Hence, the k_z -Fourier inversion acts as a spherical parametrization $\xi(k_x, k_y) : \mathcal{D}(\kappa) \rightarrow \mathcal{S}(\kappa)$ of the wavenumber support $\mathcal{S}(\kappa)$. In particular, the upper and lower hemispheres of $\mathcal{S}(\kappa)$ can be

independently parametrized on the 2D wavenumber disk $\mathcal{D}(\kappa)$, as illustrated in Fig. 2a. As a consequence, the plane-wave amplitudes are driven by the Jacobian determinant

$$J_\xi(k_x, k_y) = \sqrt{\left(\frac{\partial k_{z,0}}{\partial k_x}\right)^2 + \left(\frac{\partial k_{z,0}}{\partial k_y}\right)^2 + 1} = \frac{\kappa}{\sqrt{\kappa^2 - k_x^2 - k_y^2}} \quad (27)$$

which is obtained after substituting (19), and leads to large values near the boundary of $\mathcal{D}(\kappa)$. As shown in Fig. 2b, we also notice that h has a *bandlimited* spectrum since the coordinates (k_x, k_y) in h_\pm have a compact support $k_x^2 + k_y^2 \leq \kappa^2$ given by the disk $\mathcal{D}(\kappa)$ defined in (20). This consideration will be instrumental to derive in Section V a numerical procedure to generate spatial samples of the channel over a large, but finite, planar aperture.

As illustrated in Fig. 2b, by restricting $(k_x, k_y) \in \mathbb{R}^2$ to the support disk $\mathcal{D}(\kappa)$, only a *subset* of plane-waves in (13) effectively propagate through space, i.e., the *propagating waves*. This is a direct consequence of the Helmholtz equation, which acts as a 2D linear space-time invariant filter that cuts-off some of the propagation directions. Notice that the plane-waves associated with the propagation directions outside the disk would be associated with evanescent waves.

C. Migration Filters

Evaluating (24) over the infinite plane $z = 0$ yields $h(x, y, 0) = h_+(x, y, 0) + h_-(x, y, 0)$ with

$$h_\pm(x, y, 0) = \frac{1}{2\pi} \iint_{-\infty}^{\infty} \sqrt{S_h^\pm(k_x, k_y)} W^\pm(k_x, k_y) e^{i(k_x x + k_y y)} dk_x dk_y. \quad (28)$$

The above expression coincides with the 2D version of the Fourier spectral representation given in (13). This result is quite interesting for the following reason. By using the theory of linear-systems (reviewed in Appendix A), $h_\pm(x, y, 0)$ can be generated by passing W^\pm through a 2D linear filter with frequency response $\sqrt{S_h^\pm}$. Then, from (25) $h_\pm(x, y, z)$ can be obtained by passing $h_\pm(x, y, 0)$ through filters with wavenumber responses $e^{\pm i k_{z,0} z}$, as shown in Fig. 3. These filters are known as *propagators* or *migration filters* in the geophysical literature [1] and describe the propagation of $h(x, y, 0)$ through space along the half-spaces $z > 0$ and $z < 0$, respectively; $h(x, y, z)$ is eventually obtained as the sum of the two filter outputs.

IV. ISOTROPIC PROPAGATION

We now discuss the connection between the proposed channel model and Clarke's isotropic scattering model. Particularly, we show that the latter is the closest physically-tenable model for uncorrelated Rayleigh fading and that every non-isotropic channel can be generated by passing Clarke's isotropic channel through a linear space-time invariant filter.

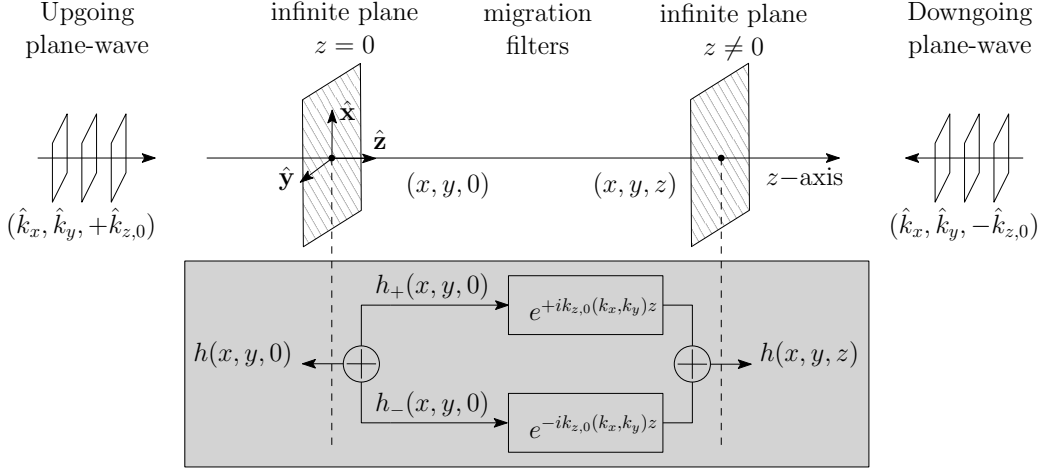


Fig. 3: Extrapolation of 3D channel through migration filters.

Definition 1 ([15]). *An isotropic channel, say $\tilde{h}(x, y, z)$, is characterized by a radially-symmetric spectral factor, which is invariant under rotations.*

This implies that we can choose the wavenumber coordinates in a convenient way such that they are aligned to one of their axes, say the k_x -axis. We may thus write

$$A_{\tilde{h}}(k_x, k_y, k_z) = A_{\tilde{h}}\left(\sqrt{k_x^2 + k_y^2 + k_z^2}, 0, 0\right) = A_{\tilde{h}}(\kappa) \quad (29)$$

where $A_{\tilde{h}}$ is the spectral factor associated with the isotropic channel. By assuming that the overall power of \tilde{h} is normalized to 1, in Appendix B it is shown that

$$A_{\tilde{h}}(\kappa) = \frac{2\pi}{\sqrt{\kappa}}. \quad (30)$$

By using (29) into (16), the power spectral density of \tilde{h} becomes

$$S_{\tilde{h}}(k_x, k_y, k_z) = \frac{4\pi^2}{\kappa} \delta(k_x^2 + k_y^2 + k_z^2 - \kappa). \quad (31)$$

Substituting (30) into (24)-(25) yields $\tilde{h}(x, y, z) = \tilde{h}_+(x, y, z) + \tilde{h}_-(x, y, z)$ with

$$\tilde{h}_{\pm}(x, y, z) = \frac{1}{2\sqrt{\pi\kappa}} \iint_{\mathcal{D}(\kappa)} \frac{e^{i(k_x x + k_y y \pm \sqrt{\kappa^2 - k_x^2 - k_y^2} z)}}{(\kappa^2 - k_x^2 - k_y^2)^{1/4}} W^{\pm}(k_x, k_y) dk_x dk_y \quad (32)$$

where W^{\pm} are two independent 2D Gaussian white noise fields with unit variance. Although (29) implies that each plane-wave carries equal power, after the Fourier inversion along κ_z , the power carried by each plane-wave in (32) is no longer constant. This is due to the spherical parametrization discussed above for the generic non-isotropic case. The evaluation of $\tilde{h}(x, y, z)$ at $z = 0$ yields the 2D Fourier spectral representation

$$\tilde{h}(x, y, 0) = \frac{1}{2\pi} \iint_{-\infty}^{\infty} \sqrt{S_{\tilde{h}}(k_x, k_y)} W(k_x, k_y) e^{i(k_x x + k_y y)} dk_x dk_y \quad (33)$$

where W is either W^+ or W^- and the power spectral density is of the form

$$S_{\tilde{h}}(k_x, k_y) = \frac{4\pi/\kappa}{\sqrt{\kappa^2 - k_x^2 - k_y^2}}, \quad (k_x, k_y) \in \mathcal{D}(\kappa) \quad (34)$$

which is a bandlimited integrable singularly spectrum that guarantees convergence of the integral representation in (33). The autocorrelation function of \tilde{h} can be computed in closed-form.

Lemma 2. *If the channel is isotropic with $A_{\tilde{h}}(\kappa) = 2\pi/\sqrt{\kappa}$, then the 3D inverse Fourier transform of the spectrum yields the explicit autocorrelation function⁶*

$$c_{\tilde{h}}(x, y, z) = \text{sinc}\left(\frac{2R}{\lambda}\right) = \frac{\sin(\kappa R)}{\kappa R} \quad (35)$$

where $R = \sqrt{x^2 + y^2 + z^2}$ is the distance among any pair of spatial points.

Proof. The proof is given in Appendix C. \square

When the 3D isotropic channel is observed over an infinite line, e.g., along the x -axis, the autocorrelation function of \tilde{h} can be computed (due to its cylindrical symmetry) on any infinitely-large plane including the receiving line (e.g., the xy -plane). By choosing

$$A_{\tilde{h}}(\kappa) = 2\sqrt{\pi} \quad (36)$$

for normalization purpose (see Appendix B), we obtain the 1D Fourier spectral representation

$$\tilde{h}(x) = \frac{1}{\sqrt{2\pi}} \int_{-\infty}^{\infty} \sqrt{S_{\tilde{h}}(k_x)} W^{\pm}(k_x) e^{ik_x x} dk_x \quad (37)$$

where W^{\pm} are two independent 1D Gaussian white noise fields with unit variance and the bandlimited integrable singularly spectrum is of the form

$$S_{\tilde{h}}(k_x) = \frac{1}{\sqrt{\kappa^2 - k_x^2}}, \quad k_x \in [-\kappa, \kappa]. \quad (38)$$

The autocorrelation function of \tilde{h} can be computed in closed-form.

Lemma 3. *If the channel is isotropic with $A_{\tilde{h}}^2(\kappa) = 4\pi$ (see Appendix B), then the autocorrelation function is*

$$c_{\tilde{h}}(x, y) = J_0\left(\frac{2\pi R}{\lambda}\right) \quad (39)$$

where $R = \sqrt{x^2 + y^2}$, and $J_0(x)$ is the Bessel function of first kind and order 0.

Proof. The proof is sketched at the end of Appendix C. \square

⁶The functional dependence on the distance R between every pair of points is a standard property of isotropic random fields [33].

Lemma 2 and Lemma 3 show that $c_{\tilde{h}}$ is the same autocorrelation function obtained by respectively using the 3D [27] and 2D [26] Clarke's model. The same results are obtained by using a “diffusion approximation” in [25]. Hence, the tools developed so far allow to study physics-based channel models in their most general form, while begin in agreement with previous results. Next, we also explain why the isotropic propagation model should be considered as the closest physically-tenable model for describing uncorrelated Rayleigh fading.

A. Rayleigh Fading Channel

With uncorrelated Rayleigh fading, the channel is modeled as a collection of i.i.d. zero-mean, Gaussian random variables for every $(x, y, z) \in \mathbb{R}^3$. This leads directly to an autocorrelation function $c_h(x, y, z) = S_0 \delta(x)\delta(y)\delta(z)$ and, in turn, to a power spectral density $S_h(k_x, k_y, k_z) = S_0$ for $(k_x, k_y, k_z) \in \mathbb{R}^3$. Hence, the uncorrelated Rayleigh fading model violates the physics principle of scalar wave propagations, which requires S_h to be impulsive. However, it is interesting to note that this model corresponds to the limit $\lambda \rightarrow 0$ ($\kappa \rightarrow \infty$).

Corollary 1. *The samples of the isotropic channel become asymptotically mutually uncorrelated as $\lambda \rightarrow 0$ ($\kappa \rightarrow \infty$) with*

$$c_{\tilde{h}}(x, y, z) = \delta(R) = \delta(x)\delta(y)\delta(z). \quad (40)$$

Proof. The proof relies on the representation of the Dirac delta through the normalized sinc(\cdot) function, i.e., $\lim_{a \rightarrow 0} \text{sinc}(R/a)/a \rightarrow \delta(R)$ with $a = \lambda/2$.⁷ \square

B. Linear system-theoretic interpretation

By using (34), we can rewrite (22) as follows

$$S_h^{\pm}(k_x, k_y) = \left(\frac{A_{h,\pm}^2(k_x, k_y)}{(4\pi)^2/\kappa} \right) S_{\tilde{h}}(k_x, k_y) \quad (41)$$

which implies that we can generate any channel h with an arbitrary spectrum by passing an isotropic channel \tilde{h} through a 2D linear space-time invariant filter with wavenumber response given by the spectral factor (up to a normalization factor). Hence, the term between brackets in (41) can be interpreted as the spatial frequency response of a shaping-filter that turns \tilde{h} into h ; see Fig. 4. This is the system-theoretic importance of the isotropic model for generating any scattering NLoS

⁷This limit must be interpreted in the distribution sense, that is, $\lim_{a \rightarrow 0} \int_{-\infty}^{\infty} \frac{1}{a} \text{sinc}(\frac{R}{a}) \varphi(R) dR = \int_{-\infty}^{\infty} \delta(R) \varphi(R) dR = \varphi(0)$ for some infinitely differentiable function $\varphi(R)$.

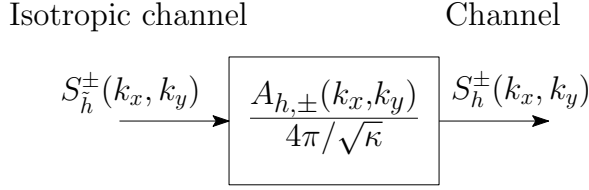


Fig. 4: Linear system-theoretic interpretation of wave propagation through scattering.

channel. Similarly to a generic h , \tilde{h} can be obtained by passing \tilde{h}_\pm in (33) through the corresponding migration filters $e^{\pm ik_z, 0z} = e^{\pm i\sqrt{\kappa^2 - k_x^2 - k_y^2}z}$ as shown in Fig. 3.

V. NUMERICAL GENERATION OF CHANNEL SAMPLES

In the above sections, we have shown that every non-isotropic physics-based channel h (i.e., that satisfies the Helmholtz equation) is a bandlimited random field with wavenumber support $\mathcal{D}(\kappa)$ and can be obtained from a bandlimited isotropic channel \tilde{h} through a linear space-time invariant filtering operation (see Fig. 4). In turn, isotropic channels $\tilde{h}(x, y, 0)$ observed over an *infinitely-large* spatially-continuous plane $z = 0$ are described by the 2D Fourier spectral representation in (32). The evaluation of $\tilde{h}(x, y, z)$ over any infinite z -plane is implemented by passing $\tilde{h}(x, y, 0)$ through migration filters, as shown in Fig. 3. All this is instrumental to develop a numerical procedure to efficiently generate channel samples over *large, but finite*, spatially-constrained rectangular apertures (i.e., linear, planar, and volumetric apertures).

A. Fourier Plane-Wave Series Representation of Isotropic Channels

Consider a large, but finite, spatially-continuous planar aperture $\mathcal{V} = \{(x, y) \in \mathbb{R}^2 : x \in [0, L_x], y \in [0, L_y]\}$ of side lengths $L_x < \infty$ and $L_y < \infty$. The same procedure described in Appendix D-A to obtain a Fourier series expansion approximation of a bandlimited random process with $\omega \in [-\Omega, \Omega]$ over a finite time interval $t \in [0, T]$ can be extended to isotropic spatial random fields observed over a spatially-continuous rectangle. This is obtained by replacing the time-frequency mapping with its space-wavenumber counterpart. To do so, the time interval $t \in [0, T]$ must be substituted with the spatial interval $(x, y) \in \mathcal{V}$, and the angular frequency interval $\omega \in [-\Omega, \Omega]$ with the wavenumber disk $(k_x, k_y) \in \mathcal{D}(\kappa)$ with $\kappa = 2\pi/\lambda$. In analogy with frequency-domain discretization of a random process, we partition the spectral disk $\mathcal{D}(\kappa)$ uniformly with wavenumber spacing intervals $2\pi/L_x$ and $2\pi/L_y$ so that each partition is indexed by

$$\mathcal{E} = \{(\ell, m) \in \mathbb{Z}^2 : (\ell\lambda/L_x)^2 + (m\lambda/L_y)^2 \leq 1\} \quad (42)$$

which is a 2D lattice ellipse of semi-axes L_x/λ and L_y/λ . Hence, in the same way (57) can be approximated over $t \in [0, T]$ with (70) as $\Omega T \rightarrow \infty$, (33) can be approximated over \mathcal{V} as $\min(L_x, L_y)/\lambda \rightarrow \infty$ by

$$\tilde{h}(x, y) \approx \sum_{(\ell, m) \in \mathcal{E}} H_{\ell m} e^{i2\pi\left(\frac{\ell x}{L_x} + \frac{m y}{L_y}\right)}, \quad (x, y) \in \mathcal{V} \quad (43)$$

where $H_{\ell m} \sim \mathcal{N}_{\mathbb{C}}(0, \sigma_{\ell m}^2)$ are statistically-independent Gaussian-distributed random variables with variances $\sigma_{\ell m}^2$ as computed in Appendix D-C. By using the Fourier harmonics interpretation in terms of plane-waves developed throughout this paper, we can refer to (43) as the *Fourier plane-wave series representation*. This representation takes the form of a superposition of a *countably-finite* number of plane-waves having statistically-independent Gaussian-distributed random amplitudes and provides an approximation of $\tilde{h}(x, y)$ by a 2D *periodic* stationary random field over its fundamental period \mathcal{V} . Remarkably, the comparison between (32) and (43) reveals that when the reception of a complex-valued electromagnetic field takes place over a large, but finite, rectangle only a discrete subset of propagating plane-waves within $\mathcal{D}(\kappa)$ are effectively resolved at the receiver.

The Fourier plane-wave series representation of $\tilde{h}(x, y, z)$ over any compact z -plane can be implemented by using migration filters having wavenumber responses $e^{\pm i\kappa_{z, \ell m} z}$ with

$$\kappa_{z, \ell m} = \sqrt{\kappa^2 - \left(\frac{2\pi\ell\lambda}{L_x}\right)^2 - \left(\frac{2\pi m\lambda}{L_y}\right)^2} = 2\pi\sqrt{1 - \left(\frac{\ell}{L_x/\lambda}\right)^2 - \left(\frac{m}{L_y/\lambda}\right)^2} \quad (44)$$

as obtained from (19) by evaluating (κ_x, κ_y) at $\left(\frac{2\pi\ell}{L_x}, \frac{2\pi m}{L_y}\right)$. The representation in (43) becomes

$$\tilde{h}(x, y, z) \approx \sum_{(\ell, m) \in \mathcal{E}} H_{\ell m}(z) e^{i2\pi\left(\frac{\ell x}{L_x} + \frac{m y}{L_y}\right)}, \quad (x, y, z) \in \mathcal{V} \quad (45)$$

where

$$H_{\ell m}(z) = H_{\ell m}^+ e^{i\kappa_{z, \ell m} z} + H_{\ell m}^- e^{-i\kappa_{z, \ell m} z} \quad (46)$$

and $H_{\ell m}^\pm \sim \mathcal{N}_{\mathbb{C}}(0, \sigma_{\ell m}^2/2)$. Next, (45) is used to develop a numerical procedure to efficiently generate channel samples over large, but finite, spatially-constrained rectangular apertures (i.e., linear, planar, and volumetric apertures).

B. Volumetric Aperture

We observe that each realization of \tilde{h} in (45) is nothing but a 2D inverse discrete-wavenumber Fourier transform of dimension $4L_x L_y / \lambda^2$. Thus, the spatial samples of \tilde{h} can be generated simply through a 2D inverse discrete Fourier transform. Let us uniformly discretize the 3D continuous aperture \mathcal{V} on a spatial grid $\mathcal{V}_N = \{(x, y, z)_n \in \mathcal{V} : n = 1, \dots, N\}$ of $N = N_x N_y N_z$ points so that

$N_x = \lceil L_x / \Delta_x \rceil$, $N_y = \lceil L_y / \Delta_y \rceil$, and $N_z = \lceil L_z / \Delta_z \rceil$ with spacing Δ_x , Δ_y , and Δ_z along the three Cartesian axis. In each channel realization, we can generate spatial samples of $\tilde{h}((x, y, z) \in \mathcal{V}_N)$ as

$$\tilde{h}_N(x_n, y_j, z_k) \approx \sum_{(\ell, m) \in \mathcal{E}} \sum H_{\ell m}(z_k) e^{i2\pi \left(\frac{\ell}{N_x} + \frac{m}{N_y} \right)}, \quad n = -\frac{N_x}{2}, \dots, \frac{N_x}{2} - 1, \quad j = -\frac{N_y}{2}, \dots, \frac{N_y}{2} - 1. \quad (47)$$

Also, by choosing N to be an integer power of 2, a computationally efficient way of generating spatial samples of \tilde{h} through IFFT algorithms [38] is leveraged. Moreover, every realization of \tilde{h} is bandlimited with 2D spectral support $\mathcal{D}(\kappa)$. The Nyquist sampling condition for a bandwidth of $2\kappa = 4\pi/\lambda$ (along both the x - and y -axis) requires

$$\min(\Delta_x, \Delta_y) \leq \frac{2\pi}{2\kappa} = \frac{\lambda}{2}. \quad (48)$$

Hence, the conventional half-wavelength antenna spacing is in general adequate to generate spatial samples of the channel. As a consequence, a half-wavelength array can be seen as obtained from a spatially-continuous aperture with Nyquist sampling at $\lambda/2$ intervals. Notice that unlike Δ_x and Δ_y , the spatial sampling interval Δ_z along the z -axis can be chosen arbitrarily. When IFFT algorithms are applied [38], the overall complexity is of order $\mathcal{O}(N \log(N_x N_y))$ which accounts for the cost of computing a 2D $N_x N_y$ -points IFFT for each of the N_z samples.

To summarize, Fig. 5 depicts the block diagram of the Fourier plane-wave series representation in (45). To generate spatial samples of the channel $h(x_n, y_j, z_k)$ at any plane $z_k = \text{const.}$, one needs to: *i*) generate two 2D independent Gaussian random lattice field $\{H_{\ell m}^{\pm}\}$, with variances $\{\sigma_{\ell m}^2\}$ as computed in Appendix D-C; *ii*) pass the isotropic lattice fields through a pair of 2D spatial filters with frequency response $A_{h, \pm}(k_x, k_y)/(4\pi/\kappa)$ with (κ_x, κ_y) being evaluated at $\left(\frac{2\pi\ell}{\lambda L_x}, \frac{2\pi m}{\lambda L_y}\right)$; *iii*) apply the migration filters for every $z_k = k\Delta_z$ with arbitrary Δ_z and sum them up; *iv*) pass the generated lattice field $\{H_{\ell m}(z_k)\}$ through a 2D $N_x N_y$ -point IFFT.

C. Planar Aperture

The Fourier plane-wave series representation of $\tilde{h}(x, y) = \tilde{h}(x, y, 0)$ over a rectangular aperture $\mathcal{V} = \{(x, y) \in \mathbb{R}^2 : x \in [0, L_x], y \in [0, L_y]\}$ of side lengths $L_x < \infty$ and $L_y < \infty$ is given by (43). Given a 2D uniform spatial grid $\mathcal{V}_N = \{(x, y)_n \in \mathcal{V} : n = 1, \dots, N\}$ of $N = N_x N_y$ points such that $N_x = \lceil L_x / \Delta_x \rceil$ and $N_y = \lceil L_y / \Delta_y \rceil$ with spacing Δ_x and Δ_y along the x - and y -axis, respectively. A computationally efficient way of generating channel samples of $\tilde{h}((x, y) \in \mathcal{V}_N)$ is given by (47) by evaluating the Fourier random coefficients $H_{\ell m}(z_k)$ at $z_k = 0$. The overall complexity is of order $\mathcal{O}(N \log(N))$ that includes the cost of computing a 2D N -points IFFT.

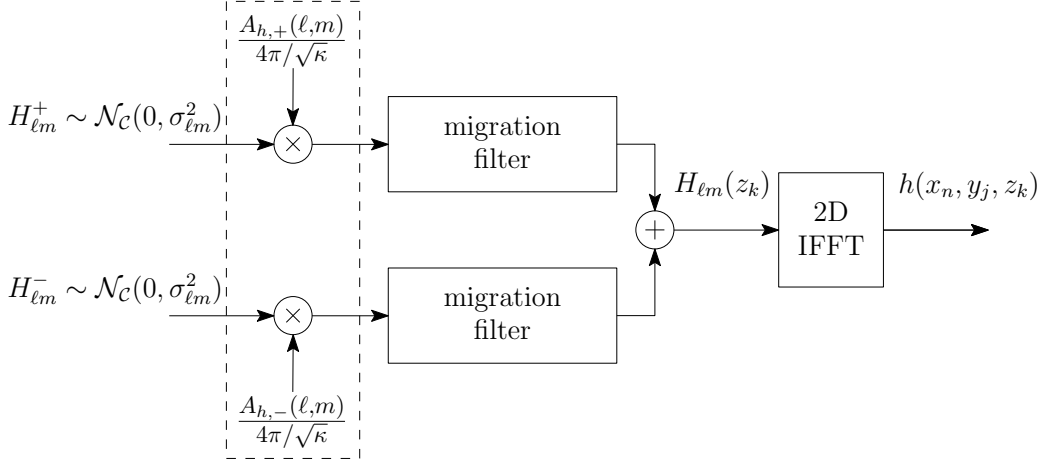


Fig. 5: Block diagram of the numerical generation procedure of spatial channel samples.

D. Linear Aperture

The restriction to a linear aperture $\mathcal{V} = \{x \in \mathbb{R} : x \in [0, L_x]\}$ of side length $L_x < \infty$ squeezes the 2D disk $\mathcal{D}(\kappa)$ to the k_x -axis so that the wavenumber support becomes a 1D segment $k_x \in [0, \kappa]$ as shown in (38). By partitioning the spectral segment uniformly with wavenumber spacing interval $2\pi/L_x$ so that each partition is indexed by $\ell = \{-L_x/\lambda, \dots, L_x/\lambda - 1\}$, the Fourier plane-wave series representation of $\tilde{h}(x) = \tilde{h}(x, 0, 0)$ over \mathcal{V} becomes a 1D inverse discrete Fourier transform:

$$\tilde{h}(x) \approx \sum_{\ell=-L_x/\lambda}^{L_x/\lambda-1} H_\ell e^{i2\pi \frac{\ell x}{L_x}}, \quad x \in \mathcal{V} \quad (49)$$

where $H_\ell \sim \mathcal{N}_C(0, \sigma_\ell^2)$ are statistically-independent Gaussian-distributed random variables with variances σ_ℓ^2 as computed in Appendix D-C. Given a 1D uniform spatial grid $\mathcal{V}_N = \{x_n \in \mathcal{V} : n = 1, \dots, N\}$ of $N = \lceil L_x/\Delta_x \rceil$ points with spacing Δ_x , we can efficiently generate samples of $\tilde{h}(x \in \mathcal{V}_N)$ through a 1D IFFT as

$$\tilde{h}_N(x_n) \approx \sum_{\ell=-L_x/\lambda}^{L_x/\lambda-1} H_\ell e^{i2\pi \ell n / N}, \quad n = -\frac{N}{2}, \dots, \frac{N}{2} - 1 \quad (50)$$

where Δ_x is chosen according to the Nyquist sampling condition for a 2κ -bandlimited process

$$\Delta_x \leq \frac{\lambda}{2}. \quad (51)$$

The overall complexity of the channel generation procedure is of order $\mathcal{O}(N \log(N))$.

E. Numerical Validation

Numerical results are now used to validate the accuracy of the analytical framework developed above. We approximate the continuous aperture by discretizing it on the spatial grid \mathcal{V}_N of N points.

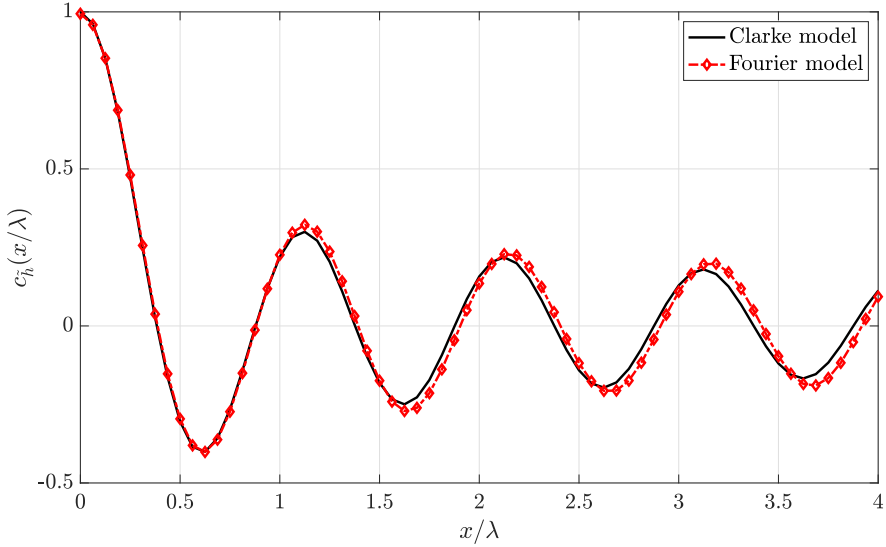


Fig. 6: 1D autocorrelation as a function of $x/\lambda \in [0, L_x/4]$ with $L_x = 16\lambda$, and $\Delta_x = \lambda/16$.

We focus on the isotropic propagation scenario since it is the key to generate any non-isotropic channels. The isotropic channel samples are generated as shown above for any $(x, y, z)_n \in \mathcal{V}_N$ and then collected into a random vector $\tilde{\mathbf{h}}_N \in \mathbb{C}^N$. The accuracy of the proposed method is compared to the conventional discrete Karhunen-Loëve representation; that is, $\tilde{\mathbf{h}}_N = \mathbf{C}_{\tilde{h}}^{1/2} \mathbf{e}$ where $\mathbf{e} \sim \mathcal{N}_{\mathbb{C}}(\mathbf{0}, \mathbf{I}_N)$, and $\mathbf{C}_{\tilde{h}} \in \mathbb{C}^{N \times N}$ is the spatial correlation matrix. This matrix is computed by sampling Clarke's autocorrelation function [26], [27], which for a planar/volumetric aperture is given by $c_h(R) = J_0(2\pi R/\lambda)$ (see Lemma 3), whereas it reduces to $c_h(R) = \text{sinc}(2R/\lambda)$ (see Lemma 2) with linear apertures. In general, $\mathbf{C}_{\tilde{h}}$ is semidefinite positive and has a symmetric block-Toeplitz structure with entries $[\mathbf{C}_h]_{nm} = c_h(R_{nm})$ with $n, m = 1, \dots, N$, where $R_{nm} = \|\mathbf{r}_n - \mathbf{r}_m\|$ is the distance between grid points $\mathbf{r}_n = (x, y, z)_n \in \mathcal{V}_N$ and $\mathbf{r}_m = (x, y, z)_m \in \mathcal{V}_N$. By choosing a uniform spacing Δ along the x - and y -axis, this matrix becomes of symmetric Toeplitz structure and it is therefore fully characterized by its first row (or column). Hence, we compare these two methods by plotting the first row of their corresponding spatial correlation matrices.

We begin by considering a linear aperture with $L_x = 16\lambda$. Fig. 6 illustrates the 1D autocorrelation function of the numerically generated samples $\tilde{h}(x_n)$ with spatial sampling $\Delta = \lambda/16$. As it is seen, the empirical autocorrelation function matches well its closed form, which is known a priori and given by $c_{\tilde{h}}(R) = J_0\left(\frac{2\pi R}{\lambda}\right)$ with $R = x$. This validates the accuracy of the numerical procedure developed above for the 2D propagation model and the applicability of the Fourier plane-wave spectral representation to model the channel over finite rectangular apertures.

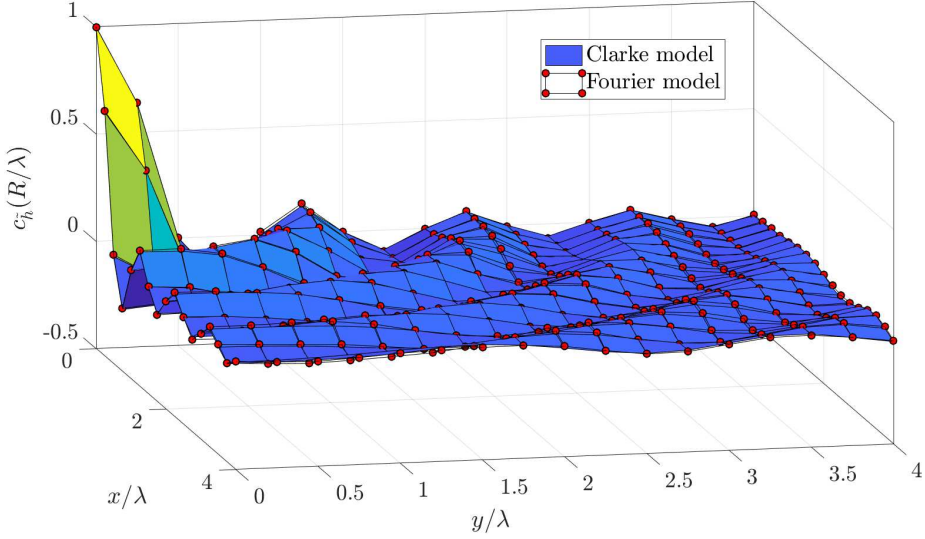


Fig. 7: 2D autocorrelation evaluated at $z = 0$ as a function of $x/\lambda \in [0, L_x/4]$ and $y/\lambda \in [0, L_y/4]$ with $L_x = L_y = 16\lambda$, and $\Delta_x = \Delta_y = \lambda/4$.

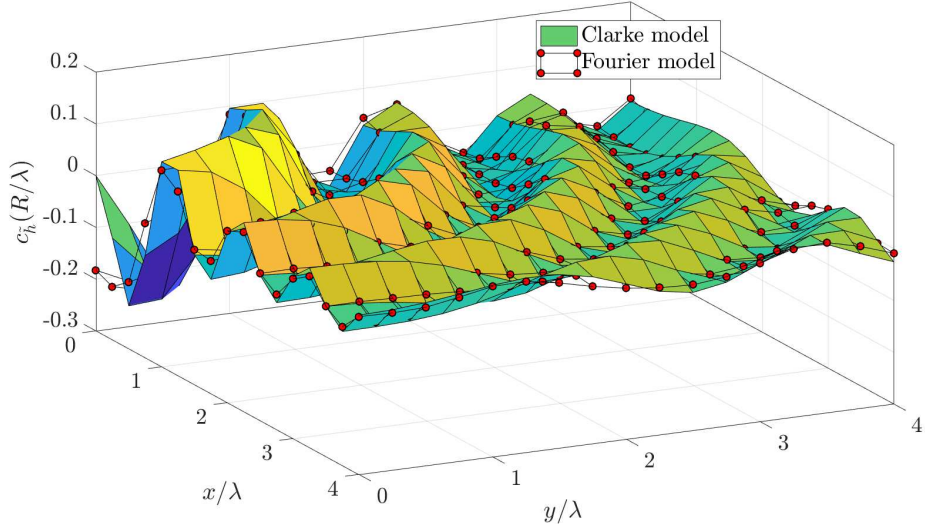


Fig. 8: 2D autocorrelation evaluated at $z/\lambda = 1/2$ as a function of $x/\lambda \in [0, L_x/4]$ and $y/\lambda \in [0, L_y/4]$ with $L_x = L_y = 16\lambda$, and $\Delta_x = \Delta_y = \lambda/4$.

Fig. 7 plots the 2D autocorrelation function of $\tilde{h}_N(x_n, y_j, 0)$ over a rectangular grid on the plane $z_k = 0$ of side lengths $L_x = L_y = 16\lambda$ with uniform spacing $\Delta = \lambda/4$. Similar conclusions as for 1D apertures hold true. Finally, Fig. 8 validates the effect of migration filters to obtain the 2D autocorrelation function of $\tilde{h}_N(x_n, y_j, z_k)$ over the same rectangular grid on the plane $z_k = \lambda/2$.

VI. DISCUSSION AND OUTLOOK

We modeled the 3D small-scale fading as a zero-mean, spatially-stationary, complex-Gaussian and scalar random field, that satisfies the homogeneous Helmholtz equation. The power spectral density is given by the product between a Dirac delta function, which constrains the spatial frequency support on the surface of an impulsive sphere of radius $\kappa = 2\pi/\lambda$, and a non-negative amplitude term that defines directional weighting. Consequently, the 3D small-scale fading is fundamentally 2D in its underlying structure and have bandlimited spectra enclosed within a disk of radius κ . This is due to the Helmholtz equation that was shown to be an extremely strong linear space-time invariant physical filter that constraint. We derived a statistical Fourier description of the 3D small-scale fading taking the form of a 2D plane-wave spectral representation having statistically independent Gaussian-distributed random amplitudes. This is generated as a linear combination of all-pass filtered versions of two independent 2D random fields. Suitably discretized, the Fourier spectral representation provided an accurate and computationally tractable numerical procedure to generate spatial samples of small-scale fading over spatially-contained continuous apertures.

Our treatment can be extended to the more general case of vector electromagnetic random fields wherein each of its Cartesian components is a function of seven scalar variables: the temporal frequency ω (or equivalently the time t), and six Cartesian coordinates that denote the spatial positions of transmitter and receiver [1]. We anticipate that the proposed analytical framework leads to an inverse procedure to efficiently evaluate the joint likelihood of the channel's noisy measurements over continuous rectangular apertures [1]. This will prove to be a valuable tool for the theoretical analysis of Holographic MIMO as well as of any spatially-constrained MIMO system with closely-spaced antennas. For example, it can be used to determine the upper limit to the available degrees of freedom [39]. Particularly, it turns out that, for a closed region of space, this is proportional to the area of the surface of the region, measured in units of wavelengths-squared, and not the volume (as it would be with Rayleigh fading channel). This result is in agreement with [40], [41] and imposes a limit on the number of parallel channels that can be established on a communication link.

APPENDIX A

REVIEWING THE FOURIER SPECTRAL REPRESENTATION

Every zero-mean, second-order, stationary random process $y(t)$ with power spectral density $S_y(\omega)$ can be represented through its Fourier spectral representation [32, Eq. (223)]:

$$y(t) = \frac{1}{\sqrt{2\pi}} \int_{-\infty}^{\infty} e^{i\omega t} dY(\omega) \quad (52)$$

where the integral must be interpreted in the stochastic mean-square sense and $Y(\omega)$ is the integrated Fourier transform of $y(t)$; that is, it is a Wiener process such that in differential form $\mathbb{E}\{dY(\omega)dY^*(\omega')\} = 0$ for $\omega \neq \omega'$ and

$$\mathbb{E}\{|dY(\omega)|^2\} = \frac{d\omega}{2\pi} S_y(\omega) \quad (53)$$

where $dY(\omega)$ is the increment integrated Fourier transform [32, Sec. 3.6]. To rewrite (52) as a function of $S_y(\omega)$, we can proceed as follows. Take a stationary random process $x(t)$ with power spectral density $S_x(\omega)$ and pass it through a linear time-invariant system with arbitrary frequency response $F(\omega)$. The output $y(t)$ is a random process such that (in terms of the increment integrated Fourier transforms) [32, Eq. (233)]

$$dY(\omega) = dX(\omega)F(\omega) \quad (54)$$

from which it follows that $\mathbb{E}\{|dY(\omega)|^2\} = |F(\omega)|^2 \mathbb{E}\{|dX(\omega)|^2\}$ with $\mathbb{E}\{|dX(\omega)|^2\} = \frac{d\omega}{2\pi} S_x(\omega)$. Combing this result with (53) yields $S_y(\omega) = S_x(\omega)|F(\omega)|^2$ from which

$$F(\omega) = \sqrt{S_y(\omega)/S_x(\omega)}. \quad (55)$$

From (52), by plugging (55) into (54), it follows that we can generate $y(t)$ with a given power spectrum $S_y(\omega)$ by passing a stationary white-noise random process $x(t)$ (i.e., with $S_x(\omega) = 1$ for $\omega \in \mathbb{R}$) through a linear time-invariant filter with frequency response $F(\omega) = \sqrt{S_y(\omega)}$. This provides us with the linear-system form of the Fourier spectral representation

$$y(t) = \frac{1}{\sqrt{2\pi}} \int_{-\infty}^{\infty} \sqrt{S_y(\omega)} e^{i\omega t} dX(\omega). \quad (56)$$

The Riemann integral form of (56) reads as⁸

$$y(t) = \frac{1}{\sqrt{2\pi}} \int_{-\infty}^{\infty} \sqrt{S_y(\omega)} W(\omega) e^{i\omega t} d\omega \quad (57)$$

⁸In general, a Riemann-Stieltjes integral is equal to its Riemann counterpart if the integrator function is continuously differentiable over $\omega \in \mathbb{R}$. This, however, is not true for the integral in (56) since each realization of the Wiener process $X(\omega)$ is continuous everywhere, but nowhere differentiable with probability 1 [32].

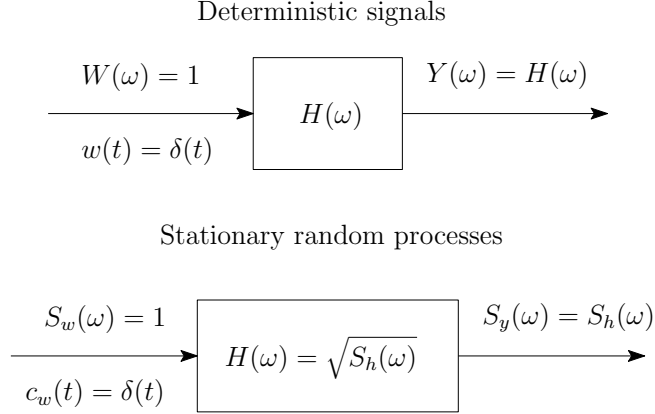


Fig. 9: Analogy between Dirac delta function and white noise in linear systems.

where $W(\omega)$ is a white-noise Gaussian process with unit spectrum, which can be seen as a superposition of an *uncountably-infinite* number of harmonics having statistically-independent Gaussian-distributed random coefficients. The above spectral representation finds its justification through the linear functional of a white-noise random process $W(\omega)$ with a complex-valued \mathcal{L}_2 function [35, Sec. 7.4]. In fact, $W(\omega)$ can be viewed as a generalized random process with $c_W(\omega) = \mathbb{E}\{W(\omega + \omega')W^*(\omega')\} = \delta(\omega)$ [35, Sec. 7.7] in the same manner the Dirac delta function can be viewed as a generalized function, or distributions [34]. In other words, a white-noise process can be regarded as the stochastic counterpart to the Dirac delta function, which provides us with a system-theoretic interpretation of (57). This implies that the generation of a random process with a given power spectral density is analogous to the generation of a deterministic signal with a given Fourier transform; see Fig. 9.

The generalization of (57) to spatially-stationary random fields reads as (13) (see [30, Eq. (2.12)] for its Riemann-Stieltjes version), which is perfectly rigorous since both Fourier transform of multivariate signals and Dirac delta function in higher dimensions are perfectly defined.

APPENDIX B POWER NORMALIZATION

Assume that $\tilde{h}(x, y, z)$ has unit power, i.e., $1/(2\pi)^3 \iiint_{-\infty}^{\infty} S_{\tilde{h}}(k_x, k_y, k_z) dk_x dk_y dk_z = 1$. By substituting (29) into (16), we obtain the following condition

$$A_h^2(\kappa) = \frac{(2\pi)^3}{\iiint_{-\infty}^{\infty} \delta(k_x^2 + k_y^2 + k_z^2 - \kappa^2) dk_x dk_y dk_z}. \quad (58)$$

The above integral can be solved by a change of integration variables to spherical coordinates

$$\int_0^{2\pi} \int_0^\pi \int_0^\infty \delta(k_r^2 - \kappa^2) k_r^2 \sin(k_\theta) dk_\phi dk_\theta dk_r = 4\pi \int_0^\infty \delta(k_r^2 - \kappa^2) k_r^2 dk_r \quad (59)$$

where we have used $\int_0^{2\pi} \int_0^\pi \sin(k_\theta) dk_\phi dk_\theta = 4\pi$. We now observe that [37, Eq. 181.a]

$$\delta(k_r^2 - \kappa^2) = \frac{\delta(k_r - \kappa) + \delta(k_r + \kappa)}{2\kappa} \quad (60)$$

which substituted into (59) yields $2\pi\kappa$, where we picked up the positive zero only. The normalizing spectral factor is thus given by $A_h^2(\kappa) = 4\pi^2/\kappa$. The spectral factor for an isotropic 2D channel can be obtained by following the same arguments above by using polar coordinates instead.

APPENDIX C

PROOF OF LEMMA 2

The substitution of (31) into (11) yields the autocorrelation function of an isotropic channel

$$c_{\tilde{h}}(x, y, z) = \frac{1}{4\pi\kappa} \iiint_{-\infty}^{\infty} \delta(k_x^2 + k_y^2 + k_z^2 - \kappa^2) e^{i(k_x x + k_y y + k_z z)} dk_x dk_y dk_z. \quad (61)$$

The above integral is a 3D Fourier inverse transform of a spherically symmetric function $\delta(k_x^2 + k_y^2 + k_z^2 - \kappa^2)$. Thus, by aligning the spatial vector to one of the axis, say the x -axis, such that $(x, y, z) = (R, 0, 0)$ with $R = \sqrt{x^2 + y^2 + z^2}$ we obtain

$$c_{\tilde{h}}(x, y, z) = \frac{1}{2\pi\kappa} \iiint_{-\infty}^{\infty} \delta(k_x^2 + k_y^2 + k_z^2 - \kappa^2) e^{ik_x R} dk_x dk_y dk_z. \quad (62)$$

The change of integration variables from Cartesian to spherical $(k_x, k_y, k_z) \rightarrow (k_r, k_\theta, k_\psi)$ yields

$$c_{\tilde{h}}(x, y, z) = \frac{1}{2\pi\kappa} \int_0^\infty \int_0^\pi \int_0^{2\pi} \delta(k_r^2 - \kappa^2) e^{ik_r R \cos(k_\theta)} k_r^2 \sin(k_\theta) dk_r dk_\theta dk_\phi \quad (63)$$

which by using (60) and exploiting the angular symmetry over k_ϕ leads to

$$c_{\tilde{h}}(x, y, z) = \frac{1}{2} \int_0^\pi e^{i\kappa R \cos(k_\theta)} \sin(k_\theta) dk_\theta \stackrel{(a)}{=} j_0(\kappa R) \quad (64)$$

where (a) follows from Poisson's integral [42, Eq. 10.1.14] and $j_0(x)$ is the spherical Bessel function of the first kind and order 0, defined as $j_0(x) = \sin(x)/x$. The autocorrelation function of an isotropic 2D channel follows similarly from polar coordinates and the integral representation of Bessel's functions of first kind $\frac{1}{\pi} \int_0^\pi e^{iz \cos(k_\theta)} dk_\theta = J_0(z)$ [42, Eq. (9.1.21)].

APPENDIX D

A. Fourier series spectral representation

Consider a *bandlimited* zero-mean, stationary, Gaussian random process $y(t)$ of frequency bandwidth $\Omega < \infty$ and observed over an *infinitely-long* time interval $t \in (-\infty, \infty)$. Assume that $y(t)$ has an *integrable singularly* spectrum $S_y(\omega)$ with $\omega \in [-\Omega, \Omega]$ such that $\int_{-\Omega}^{\Omega} S_y(\omega) \frac{d\omega}{2\pi} < \infty$, i.e., y is a second-order random process. The frequency domain description of y is given by the Fourier spectral representation in (57) where the integration interval is limited by its bandlimited spectra.

Let us now observe y over a *large, but finite*, time interval $t \in [0, T]$ of duration $T < \infty$. We aim to provide a discrete-frequency approximation for the Fourier spectral representation over $t \in [0, T]$. We start by partitioning the integration interval uniformly with frequency spacing $\Delta_\omega = 2\pi/T$

$$y(t) = \frac{1}{\sqrt{2\pi}} \sum_{\ell=-\Omega T/\pi}^{\Omega T/\pi-1} \left(\int_{2\pi\ell/T}^{2\pi(\ell+1)/T} \sqrt{S_y(\omega)} W(\omega) e^{i\omega t} d\omega \right), \quad t \in [0, T]. \quad (65)$$

The application of the first mean-value theorem [43, Ch. 3] over each interval yields

$$y(t) \approx \frac{1}{\sqrt{2\pi}} \sum_{\ell=-\Omega T/\pi}^{\Omega T/\pi-1} \left(\int_{2\pi\ell/T}^{2\pi(\ell+1)/T} \sqrt{S_y(\omega)} W(\omega) d\omega \right) e^{i2\pi(\ell+1/2)t/T}, \quad t \in [0, T] \quad (66)$$

where the approximation error becomes negligible as $\Delta_\omega/\Omega \rightarrow 0$ (i.e., $\Omega T \rightarrow \infty$). The integral between brackets is a linear functional of a white Gaussian noise process $W(\omega)$ [35, Ch. 7.4]

$$Y_\ell = \frac{1}{\sqrt{2\pi}} \int_{2\pi\ell/T}^{2\pi(\ell+1)/T} \sqrt{S_y(\omega)} W(\omega) d\omega = \int_{-\infty}^{\infty} g_\ell(\omega) W(\omega) d\omega \quad (67)$$

with a real-valued \mathcal{L}_2 function

$$g_\ell(\omega) = \begin{cases} \sqrt{S_y(\omega)/2\pi} & \omega \in [\frac{2\pi\ell}{T}, \frac{2\pi(\ell+1)}{T}] \\ 0 & \text{elsewhere.} \end{cases} \quad (68)$$

We notice that $\{g_\ell(\omega)\}$ with $\ell \in \{-\Omega T/\pi, \dots, \Omega T/\pi - 1\}$ are such that $\int_{-\infty}^{\infty} g_\ell(\omega) g_m(\omega) d\omega = \sigma_\ell^2 \delta_{m-\ell}$ and each function has energy

$$\sigma_\ell^2 = \int_{2\pi\ell/T}^{2\pi(\ell+1)/T} S_y(\omega) \frac{d\omega}{2\pi} < \infty \quad (69)$$

which is finite for every second-order random process. Thus $\{g_\ell(\omega)\}$ form a set of orthogonal functions, or better, an orthogonal basis for the space of real-valued \mathcal{L}_2 functions. As a consequence, we can interpret (67) as the ℓ -th coordinate of an orthonormal series expansion of W over the basis $\{g_\ell(\omega)\}$. Now, the expansion of any white Gaussian noise process over an arbitrary orthogonal \mathcal{L}_2 basis of functions produces a sequence $Y_\ell \sim \mathcal{N}_{\mathbb{C}}(0, \sigma_\ell^2)$ of independent zero-mean,

circularly-symmetric Gaussian random variables with finite variances σ_ℓ^2 [35, Ch. 7.7]. Thus, we may approximate (57) for a bandlimited spectra S_y as

$$y(t) \approx \sum_{\ell=-\Omega T/\pi}^{\Omega T/\pi-1} Y_\ell e^{i2\pi(\ell+1/2)t/T} \stackrel{(a)}{\approx} \sum_{\ell=-\Omega T/\pi}^{\Omega T/\pi-1} Y_\ell e^{i2\pi\ell t/T}, \quad t \in [0, T] \quad (70)$$

where (a) holds in the statistical distribution sense and it is due the phase invariant property of circularly-symmetric Gaussian random variables. The approximation error becomes negligible as $\Omega T \rightarrow \infty$. The above formula provides an orthonormal decomposition of y taking the form of a bandlimited Fourier series expansion having a countably-finite number of statistically-independent Gaussian-distributed coefficients. Hence, it provides an approximation of y over $t \in [0, T]$ through a *periodic* stationary random process over its fundamental period $T = 2\pi/\Delta_\omega$. The convergence of (70) in mean square may be proven by recurring to the Parseval's theorem and recurring to (69)

$$\mathbb{E}\{|y(t)|^2\} = \sum_{\ell=-\Omega T/\pi}^{\Omega T/\pi-1} \sigma_\ell^2 = \int_{-\Omega}^{\Omega} S_y(\omega) \frac{d\omega}{2\pi} < \infty. \quad (71)$$

B. Connection to the Karhunen-Loève series expansion

The Fourier series expansion (70) is reminiscent of the famous Karhunen-Loève series expansion $y(t) = \sum_\ell c_\ell \varphi_\ell(t)$ with $t \in [0, T]$ where c_ℓ and φ_ℓ are the eigenvalues and eigenfunctions of such expansion. This is the continuous analog of the decomposition of a random vector into its principal components (i.e., eigenvalue decomposition) [32]. In particular, for a bandlimited random process of bandwidth Ω , (70) can be interpreted as the asymptotic version of the Karhunen-Loève series expansion [32, Sec. 3.4.6]. As the observation interval T grows large (i.e., $\Omega T \gg 1$) the eigenvalues' power $\mathbb{E}\{|c_\ell|^2\}$ approach the power spectral density S_y , and the eigenfunctions φ_ℓ become harmonics. Thus, the Fourier coefficients $\{Y_\ell\}$ and basis $\{e^{i2\pi\ell t/T}\}$ respectively assume the meaning of Karhunen-Loève's eigenvalues and eigenfunctions.

We finally notice that the direct application of the Karhunen-Loève expansion to the modeling of y would lead to a divergent series due to the evaluation of the singular spectrum S_y on its boundary. Asymptotically as $\Omega T \rightarrow \infty$, the Fourier coefficients become a continuum and both the Fourier series and Karhunen-Loève expansion tend to the Fourier spectral representation in (57).

C. Computation of variances of Fourier coefficients

The variance σ_ℓ^2 of the ℓ -th Fourier random coefficient H_ℓ in (49) is computed from (69) by replacing the time-frequency mapping with its space-wavenumber counterpart:

$$\sigma_\ell^2 = \int_{2\pi\ell/L_x}^{2\pi(\ell+1)/L_x} S_{\tilde{h}}(k_x) \frac{dk_x}{2\pi} = \int_{\ell\lambda/L_x}^{(\ell+1)\lambda/L_x} \frac{1}{\sqrt{1-k_x^2}} \frac{dk_x}{2\pi} \quad (72)$$

where we substitute the 1D power spectrum $S_{\tilde{h}}$ in (38) and use $\kappa = 2\pi/\lambda$. Since the integrand is symmetric with respect the origin, the variances corresponding to the negative indexes can be easily found by symmetry $\sigma_{-\ell-1}^2 = \sigma_\ell^2$ for $\ell = 0, 1, \dots, L_x/\lambda - 1$. By applying, e.g., the change of integration variable $k_x = \sin u$ we obtain

$$\sigma_\ell^2 = \frac{1}{2\pi} \left(\arcsin \left(\ell \frac{\lambda}{L_x} \right) - \arcsin \left((\ell + 1) \frac{\lambda}{L_x} \right) \right), \quad \ell = 0, 1, \dots, L_x/\lambda - 1. \quad (73)$$

Similarly, the variance $\sigma_{\ell,m}^2$ of the (ℓ, m) -th Fourier random coefficient $H_{\ell m}$ in (43) is given by

$$\sigma_{\ell,m}^2 = \int_{\ell\lambda/L_x}^{\ell+1\lambda/L_x} \int_{m\lambda/L_y}^{(m+1)\lambda/L_y} \frac{4\pi}{\sqrt{1 - k_x^2 - k_y^2}} \frac{dk_x}{2\pi} \frac{dk_y}{2\pi}, \quad (\ell, m) \in \mathcal{E} \quad (74)$$

where we substitute the 2D power spectrum $S_{\tilde{h}}$ in (34) and \mathcal{E} is the 2D lattice ellipse as defined in (42). The rotational symmetry of the integrand allows us to focus on the first wavenumber quadrant only, that is, $\ell = 0, 1, \dots, L_x/\lambda - 1$ and $m = 0, 1, \dots, L_y/\lambda - 1$ from which we can derive the variances in all the other quadrants. By change of integration variable, e.g., to polar coordinates $(k_x, k_y) = (k_r \cos k_\phi, k_r \sin k_\phi)$ with $k_r \in [0, 1]$ and $k_\phi \in [0, \pi/2)$, for the case $\ell \geq m$ we obtain

$$\begin{aligned} \sigma_{\ell,m}^2 = & \int_{k_{\phi,1}}^{k_{\phi,2}} \int_{\min\left(1, \frac{m\lambda}{L_y \sin k_\phi}\right)}^{\min\left(1, \frac{(\ell+1)\lambda}{L_x \cos k_\phi}\right)} \frac{4\pi k_r}{\sqrt{1 - k_r^2}} dk_r dk_\phi + \int_{k_{\phi,2}}^{k_{\phi,3}} \int_{\min\left(1, \frac{\ell\lambda}{L_x \cos k_\phi}\right)}^{\min\left(1, \frac{(\ell+1)\lambda}{L_x \cos k_\phi}\right)} \frac{4\pi k_r}{\sqrt{1 - k_r^2}} dk_r dk_\phi \\ & + \int_{k_{\phi,3}}^{k_{\phi,4}} \int_{\min\left(1, \frac{\ell\lambda}{L_x \cos k_\phi}\right)}^{\min\left(1, \frac{(m+1)\lambda}{L_y \sin k_\phi}\right)} \frac{4\pi k_r}{\sqrt{1 - k_r^2}} dk_r dk_\phi, \quad \ell \geq m \end{aligned} \quad (75)$$

where $k_{\phi,1} = \arctan\left(\frac{mL_x}{(\ell+1)L_y}\right)$, $k_{\phi,2} = \arctan\left(\frac{mL_x}{\ell L_y}\right)$, $k_{\phi,3} = \arctan\left(\frac{(m+1)L_x}{(\ell+1)L_y}\right)$, and $k_{\phi,4} = \arctan\left(\frac{(m+1)L_x}{\ell L_y}\right)$ such that $k_{\phi,1} \leq k_{\phi,2} \leq k_{\phi,3} \leq k_{\phi,4}$. Now, the integration of (75) over the radial wavenumber component yields to

$$\begin{aligned} \sigma_{\ell,m}^2 = & 4\pi \left(\int_{k_{\phi,1}}^{k_{\phi,2}} \sqrt{1 - \min\left(1, \frac{1}{a_{11}^2 \sin^2 k_\phi}\right)} dk_\phi - \int_{k_{\phi,1}}^{k_{\phi,2}} \sqrt{1 - \min\left(1, \frac{1}{a_{12}^2 \cos^2 k_\phi}\right)} dk_\phi \right. \\ & + \int_{k_{\phi,2}}^{k_{\phi,3}} \sqrt{1 - \min\left(1, \frac{1}{a_{21}^2 \cos^2 k_\phi}\right)} dk_\phi - \int_{k_{\phi,2}}^{k_{\phi,3}} \sqrt{1 - \min\left(1, \frac{1}{a_{22}^2 \cos^2 k_\phi}\right)} dk_\phi \\ & \left. + \int_{k_{\phi,3}}^{k_{\phi,4}} \sqrt{1 - \min\left(1, \frac{1}{a_{31}^2 \cos^2 k_\phi}\right)} dk_\phi - \int_{k_{\phi,3}}^{k_{\phi,4}} \sqrt{1 - \min\left(1, \frac{1}{a_{32}^2 \sin^2 k_\phi}\right)} dk_\phi \right) \end{aligned} \quad (76)$$

where $a_{11} = \frac{L_y}{\lambda m}$, $a_{12} = \frac{L_x}{\lambda(\ell+1)}$, $a_{21} = \frac{L_x}{\lambda\ell}$, $a_{22} = \frac{L_x}{\lambda(\ell+1)}$, $a_{31} = \frac{L_x}{\lambda\ell}$, and $a_{32} = \frac{L_y}{\lambda(m+1)}$. The above expression can be rewritten equivalently as

$$\begin{aligned} \sigma_{\ell,m}^2 = 4\pi & \left(\int_{\max(k_{\phi,1}, \arcsin(\frac{1}{a_{11}}))}^{\max(k_{\phi,2}, \arcsin(\frac{1}{a_{11}}))} \sqrt{1 - \frac{1}{a_{11}^2 \sin^2 k_{\phi}}} dk_{\phi} - \int_{\min(k_{\phi,1}, \arccos(\frac{1}{a_{12}}))}^{\min(k_{\phi,2}, \arccos(\frac{1}{a_{12}}))} \sqrt{1 - \frac{1}{a_{12}^2 \cos^2 k_{\phi}}} dk_{\phi} \right. \\ & + \int_{\min(k_{\phi,2}, \arccos(\frac{1}{a_{21}}))}^{\min(k_{\phi,3}, \arccos(\frac{1}{a_{21}}))} \sqrt{1 - \frac{1}{a_{21}^2 \cos^2 k_{\phi}}} dk_{\phi} - \int_{\min(k_{\phi,2}, \arccos(\frac{1}{a_{22}}))}^{\min(k_{\phi,3}, \arccos(\frac{1}{a_{22}}))} \sqrt{1 - \frac{1}{a_{22}^2 \cos^2 k_{\phi}}} dk_{\phi} \\ & \left. + \int_{\min(k_{\phi,3}, \arccos(\frac{1}{a_{31}}))}^{\min(k_{\phi,4}, \arccos(\frac{1}{a_{31}}))} \sqrt{1 - \frac{1}{a_{31}^2 \cos^2 k_{\phi}}} dk_{\phi} - \int_{\max(k_{\phi,3}, \arcsin(\frac{1}{a_{32}}))}^{\max(k_{\phi,4}, \arcsin(\frac{1}{a_{32}}))} \sqrt{1 - \frac{1}{a_{32}^2 \sin^2 k_{\phi}}} dk_{\phi} \right). \quad (77) \end{aligned}$$

where we used the fact that each of the above integrals yields non-zero value in the intervals $k_{\phi} \in [\arcsin(1/a), \pi/2]$ ($k_{\phi} \in [0, \arccos(1/a)]$), where $a > 1$ is one of the parameters listed above.

The variances $\sigma_{\ell,m}^2$ are obtained by solving the following indefinite integrals [43, Ch. 2.611]

$$\int \sqrt{1 - \frac{1}{a^2 \sin^2 k_{\phi}}} dk_{\phi} = \frac{1}{a} \arctan \left(\frac{\cos k_{\phi}}{\sqrt{a^2 \sin^2 k_{\phi} - 1}} \right) - a \arcsin \left(\frac{\cos k_{\phi}}{\sqrt{1 - 1/a^2}} \right) \quad (78)$$

$$\int \sqrt{1 - \frac{1}{a^2 \cos^2 k_{\phi}}} dk_{\phi} = -\frac{1}{a} \arctan \left(\frac{\sin k_{\phi}}{\sqrt{a^2 \cos^2 k_{\phi} - 1}} \right) + \arcsin \left(\frac{\sin k_{\phi}}{\sqrt{1 - 1/a^2}} \right). \quad (79)$$

Mathematical details are omitted for space limitations and will be provided upon request. Finally, the case $\ell < m$ can be treated similarly by exchanging $k_{\phi,2}$ and $k_{\phi,3}$ so that now $k_{\phi,2} = \arctan \left(\frac{(m+1)L_x}{(\ell+1)L_y} \right)$ and $k_{\phi,3} = \arctan \left(\frac{mL_x}{\ell L_y} \right)$, and change the integration limits of (75) accordingly, which can be again solved by following the same procedure explained above.

REFERENCES

- [1] T. Marzetta, "Spatially-stationary propagating random field model for Massive MIMO small-scale fading," in *IEEE International Symposium on Information Theory, 2018. Proceedings.*, June 2018.
- [2] T. L. Marzetta, "Noncooperative cellular wireless with unlimited numbers of base station antennas," *IEEE Trans. Wireless Commun.*, vol. 9, no. 11, pp. 3590–3600, November 2010.
- [3] T. L. Marzetta, E. G. Larsson, H. Yang, and H. Q. Ngo, *Fundamentals of Massive MIMO*. Cambridge University Press, 2016.
- [4] E. Björnson, J. Hoydis, and L. Sanguinetti, *Massive MIMO Networks: Spectral, Energy, and Hardware Efficiency*. Foundations and Trends in Signal Processing, 2017, vol. 11, no. 3-4.
- [5] E. Björnson, L. Sanguinetti, H. Wymeersch, J. Hoydis, and T. L. Marzetta, "Massive MIMO is a Reality - What is Next? Five Promising Research Directions for Antenna Arrays," *arXiv e-prints*, p. arXiv:1902.07678, Feb 2019.
- [6] H. Q. Ngo, E. G. Larsson, and T. L. Marzetta, "Energy and spectral efficiency of very large multiuser MIMO systems," *IEEE Trans. Commun.*, vol. 61, no. 4, pp. 1436–1449, April 2013.
- [7] E. Björnson, L. Sanguinetti, J. Hoydis, and M. Debbah, "Optimal design of energy-efficient multi-user MIMO systems: Is Massive MIMO the answer?" *IEEE Trans. Wireless Commun.*, vol. 14, no. 6, pp. 3059–3075, June 2015.

- [8] H. V. Cheng, E. Björnson, and E. G. Larsson, "Optimal pilot and payload power control in single-cell Massive MIMO systems," *IEEE Trans. Signal Process.*, vol. 65, no. 9, pp. 2363–2378, May 2017.
- [9] A. Ashikhmin and T. Marzetta, "Pilot contamination precoding in multi-cell large scale antenna systems," in *2012 IEEE International Symposium on Information Theory Proceedings*, July 2012, pp. 1137–1141.
- [10] E. Björnson, J. Hoydis, and L. Sanguinetti, "Massive MIMO has unlimited capacity," *IEEE Trans. Wireless Commun.*, vol. 17, no. 1, pp. 574–590, Jan 2018.
- [11] D. W. Prather, S. Shi, G. J. Schneider, P. Yao, C. Schuetz, J. Murakowski, J. C. Deroba, F. Wang, M. R. Konkol, and D. D. Ross, "Optically upconverted, spatially coherent phased-array-antenna feed networks for beam-space MIMO in 5G cellular communications," *IEEE Transactions on Antennas and Propagation*, vol. 65, no. 12, pp. 6432–6443, Dec 2017.
- [12] S. Hu, F. Rusek, and O. Edfors, "Beyond Massive MIMO: The potential of data transmission with large intelligent surfaces," *IEEE Trans. Signal Process.*, vol. 66, no. 10, pp. 2746–2758, May 2018.
- [13] E. J. Black, "Holographic beam forming and MIMO," Pivotal Commware, Tech. Rep., 12 2017. [Online]. Available: <https://pivotalcommware.com/wp-content/uploads/2017/12/Holographic-Beamforming-WP-v.6C-FINAL.pdf>
- [14] D. Tse and P. Viswanath, *Fundamentals of Wireless Communication*. Cambridge University Press, 2005.
- [15] A. Paulraj, R. Nabar, and D. Gore, *Introduction to Space-Time Wireless Communications*. Cambridge, UK: Cambridge University Press, 2003.
- [16] H. Huh, G. Caire, H. C. Papadopoulos, and S. A. Ramprashad, "Achieving "Massive MIMO" spectral efficiency with a not-so-large number of antennas," *IEEE Trans. Wireless Commun.*, vol. 11, no. 9, pp. 3226–3239, Sep. 2012.
- [17] J. Hoydis, S. ten Brink, and M. Debbah, "Massive MIMO in the UL/DL of cellular networks: How many antennas do we need?" *IEEE J. Sel. Areas Commun.*, vol. 31, no. 2, pp. 160–171, Feb. 2013.
- [18] L. Sanguinetti, E. Björnson, and A. Kammoun, "Large-system analysis of massive MIMO with optimal M-MMSE processing," *CoRR*, vol. abs/1903.09783, 2019. [Online]. Available: <http://arxiv.org/abs/1903.09783>
- [19] L. Sanguinetti, E. Björnson, and J. Hoydis, "Towards massive MIMO 2.0: Understanding spatial correlation, interference suppression, and pilot contamination," *CoRR*, vol. abs/1904.03406, 2019. [Online]. Available: <http://arxiv.org/abs/1904.03406>
- [20] A. S. Y. Poon, R. W. Brodersen, and D. N. C. Tse, "A spatial channel model for multiple-antenna systems," in *IEEE Antennas and Propagation Society Symposium, 2004.*, vol. 4, June 2004, pp. 3665–3668 Vol.4.
- [21] A. S. Y. Poon, D. N. C. Tse, and R. W. Brodersen, "Impact of scattering on the capacity, diversity, and propagation range of multiple-antenna channels," *IEEE Trans. Inf. Theory*, vol. 52, no. 3, pp. 1087–1100, March 2006.
- [22] C. Masouros, M. Sellathurai, and T. Ratnarajah, "Large-scale MIMO transmitters in fixed physical spaces: The effect of transmit correlation and mutual coupling," *IEEE Trans. Commun.*, vol. 61, no. 7, pp. 2794–2804, July 2013.
- [23] C. Masouros and M. Matthaiou, "Space-constrained Massive MIMO: Hitting the wall of favorable propagation," *IEEE Commun. Lett.*, vol. 19, no. 5, pp. 771–774, May 2015.
- [24] A. F. Molisch, *Wireless Communications, Second Edition*. Wiley, 2010.
- [25] A. L. Moustakas, H. U. Baranger, L. Balents, A. M. Sengupta, and S. H. Simon, "Communication through a diffusive medium: Coherence and capacity," *Science*, vol. 287, no. 5451, pp. 287–290, 2000.
- [26] R. H. Clarke, "A statistical theory of mobile-radio reception," *The Bell System Technical Journal*, vol. 47, no. 6, pp. 957–1000, July 1968.
- [27] T. Aulin, "A modified model for the fading signal at a mobile radio channel," *IEEE Trans. Veh. Technol.*, vol. 28, no. 3, pp. 182–203, Aug 1979.
- [28] Q. Nadeem, A. Kammoun, M. Debbah, and M. Alouini, "A generalized spatial correlation model for 3D MIMO channels based on the fourier coefficients of power spectrums," *IEEE Trans. Signal Process.*, vol. 63, no. 14, pp. 3671–3686, July 2015.
- [29] W. C. Chew, *Waves and Fields in Inhomogenous Media*. Wiley-IEEE Press, 1995.

- [30] A. B. Baggeroer, "Space/time random processes and optimum array processing," Naval Undersea Center, San Diego (CA), Tech. Rep. ADA035593, Apr. 1976. [Online]. Available: [https://apps.dtic.mil/GetTRDoc?Location=U2&docType=GetTRDoc&GetTRDocId=GetTRDocId&docIdType=GetTRDocId&docId=GetTRDocId&docIdValue=ADA035593.pdf](https://apps.dtic.mil/GetTRDoc?Location=U2&docType=GetTRDoc&GetTRDocId=GetTRDocId&docIdType=GetTRDocIdType&docId=GetTRDocId&docIdValue=ADA035593.pdf)
- [31] A. Stratton, *Principles of Digital Communication*. Wiley, 2015.
- [32] H. L. Van Trees, *Detection Estimation and Modulation Theory, Part I*. Wiley, 1968.
- [33] E. Wong and B. Hajek, *Stochastic Processes in Engineering Systems*. Springer-Verlag New York, 1985.
- [34] S. G. Johnson, "When functions have no value(s): Delta functions and distributions," March 2017. [Online]. Available: <https://math.mit.edu/~stevenj/18.303/delta-notes.pdf>
- [35] R. G. Gallager, *Principles of Digital Communication*. Cambridge University Press, 2008.
- [36] T. L. Marzetta and B. M. Hochwald, "Capacity of a mobile multiple-antenna communication link in rayleigh flat fading," *IEEE Trans. Inf. Theory*, vol. 45, no. 1, pp. 139–157, Jan 1999.
- [37] G. B. Arfken, H. J. Weber, and F. E. Harris, *Mathematical Methods for Physicists*, G. B. Arfken, H. J. Weber, and F. E. Harris, Eds. Boston: Academic Press, 2013.
- [38] M. Frigo, "A fast fourier transform compiler," in *Proceedings of the ACM SIGPLAN 1999 Conference on Programming Language Design and Implementation*, ser. PLDI '99. New York, NY, USA: ACM, 1999, pp. 169–180.
- [39] A. Pizzo, T. L. Marzetta, and L. Sanguinetti, "Degrees of freedom of Holographic MIMO channels," in *2020 IEEE International Conference on Acoustics, Speech and Signal Processing*, Submitted to 2020.
- [40] M. Franceschetti, "On Landau's eigenvalue theorem and information cut-sets," *IEEE Trans. Inf. Theory*, vol. 61, no. 9, pp. 5042–5051, Sept 2015.
- [41] A. S. Y. Poon, R. W. Brodersen, and D. N. C. Tse, "Degrees of freedom in multiple-antenna channels: a signal space approach," *IEEE Trans. Inf. Theory*, vol. 51, no. 2, pp. 523–536, Feb 2005.
- [42] M. Abramowitz and I. Stegun, *Handbook of mathematical functions*. New York, NY: Dover Publications, 1972.
- [43] I. S. Gradshteyn and I. M. Ryzhik, *Table of Integrals, Series, and Products*. Academic Press, 1965.